



# Material distribution topology optimization for boundary-effect-dominated problems: a review

Eddie Wadbro<sup>1,2</sup> · Quoc Khanh Nguyen<sup>1</sup> · Mario Setta<sup>1</sup> · Martin Berggren<sup>2</sup> · Abbas Mousavi<sup>3</sup>

Received: 2 June 2025 / Revised: 10 February 2026 / Accepted: 15 February 2026  
© The Author(s) 2026

## Abstract

This review focuses on material distribution-based topology optimization methods for boundary-effect-dominated problems. More precisely, it addresses problems where the behavior at or near the boundaries of the domain significantly influences the physics, such as problems involving boundary layers or the skin effect. While traditional topology optimization techniques have been highly successful in idealized settings, boundary-sensitive problems introduce unique challenges. We survey the historical development of relevant ideas, including fictitious-domain methods and filtering techniques, and provide a detailed account of modern approaches for handling boundary effects. Key topics include cascades of filters, multi-field representations, and methods for controlling length scale and interface sharpness. We also review specialized strategies for pressure and thermal loads, as well as recent advances in the design of coated structures and impedance-based modeling of boundary layers. This article aims to provide a comprehensive and structured overview of the field.

**Keywords** Topology optimization · Material distribution · Boundary-effect-dominated problems · Implicit boundary representation · Design-dependent loads · Coated structures · Problems with layers

## 1 Introduction

Computational design optimization aims to find the best distribution of material(s) within a given domain  $\Omega \subset \mathbb{R}^d$ . In its most basic form, the problem involves two material types. In computational design optimization, the design is typically parameterized, and an algorithm systematically evaluates the objective function for different configurations in search of the best one. The choice of parameterization critically influences the optimization outcome. Here, we limit our attention

to so-called topology optimization problems, where the connectedness and shape of the optimal design are determined as part of the optimization. Among the many challenges in topology optimization are boundary-effect-dominated problems, where boundary behavior plays a dominant role and requires special attention.

In many design optimization problems, the behavior near interfaces or boundaries critically shapes the physical response, making boundary effects a central concern. For instance, in pressure-loaded shell structures, the location and shape of the pressure boundary evolve with the design. Similarly, in heat sink optimization with surface convection, the thermal boundary conditions depend on the exposed surface area, making boundary identification essential. In acoustic and electromagnetic problems, boundary layers, skin effects, and impedance conditions significantly affect the wave propagation. Neglecting boundary effects can lead to physically inconsistent results and designs with sub-optimal performance when exposed to the true physics.

The pursuit of optimal structural design has a long and rich history, with scientific contributions at least dating back to Lagrange (n.d.), who studied the shape of columns (pillars) in the context of buckling already in the 1770s. In the early 1900s, Michell (1904) published important prin-

---

Responsible Editor: Joe Alexandersen.

---

Topical Collection: ICTAM 2024 - The centennial of ICTAM Guest Editors: J. Alexandersen, A.M. Aragón, X.S. Zhang, E. Lund, E. Wadbro, J. Kook.

---

✉ Eddie Wadbro  
eddie.wadbro@kau.se

<sup>1</sup> Department of Mathematics and Computer Science, Karlstads universitet, Universitetsgatan 2, 65188 Karlstad, Sweden

<sup>2</sup> Department of Computing Science, Umeå University, MIT-huset, 90187 Umeå, Sweden

<sup>3</sup> FLOW, Engineering Mechanics, KTH Royal Institute of Technology, Osquars backe 18, 10044 Stockholm, Sweden

ciples for low-volume truss structures, using infinitely many infinitely thin bars that are optimal with respect to weight. The pioneering work by Lions (1971) presents important principles for optimal control of partial differential equations, which inspired research in the closely related field of design optimization. As an offspring of Lions' work came pioneering papers regarding design optimization of continuum structures for model problems (Glowinski 1984; Goodman et al. 1986; Kohn and Strang 1986a,b,c). Since the seminal paper by Bendsøe and Kikuchi (1988), modern topology optimization has emerged as a powerful tool for designing high-performance structures. By modern, we refer to approaches that formulate the design problem using partial differential equations—or other high-fidelity physical models—and solve them numerically as the basis for optimization. Today, most research in topology optimization uses the material distribution method (Bendsøe 1989; Zhou and Rozvany 1991; Mlejnek 1992), which is also referred to as density-based topology optimization.

Historically, the method was developed in the context of linear elasticity, with the design unknown being either the density field or some quantity directly related to it. To emphasize the broader applicability and conceptual clarity of these methods, we prefer the term material distribution-based optimization. Bendsøe and Sigmund's (2003) monograph on the subject is a cornerstone text that provides a comprehensive overview of the core principles and methods essential for optimizing material distributions. About a decade later, Sigmund and Maute (2013) and Deaton and Grandhi (2014) presented updated surveys that outline major advances in the key methodologies and approaches, showcasing their versatility and adaptability in tackling diverse engineering challenges. Material distribution methods produce outstanding results in finding conceptual designs of components under idealized conditions. They are, for example, used to design advanced lightweight components in the automotive and aeronautical industries (Zhu et al. 2016). For load-carrying elastic structures, these methods have achieved the gigavoxel scale and have been used to design a full airplane wing (Aage et al. 2017) and the girder sections of a suspension bridge (Baandrup et al. 2020).

More recently, there has been a trend toward publishing specialized review articles that highlight diverse applications, challenges, and promising avenues for specific problem types. Alexandersen and Andreasen (2020) focus on fluid-based problems, covering various applications, such as heat transfer and fluid–structure interaction. Wu et al. (2021) categorize existing approaches for multiscale topology optimization, explaining their principles and strengths. Zhu et al. (2021) examine the interplay between topology optimization and additive manufacturing, discussing opportunities and challenges in designing components accounting for the 3D manufacturing process. Yvonnet and Da (2024) review topol-

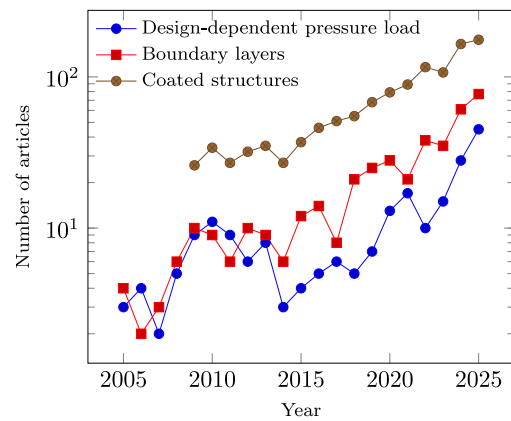


**Fig. 1** Number of publications per year in the past 20 years for design optimization problems with design-dependent pressure load, boundary layers, or coated structures

ogy optimization methods for fracture resistance, from classic stress-based approaches to modern techniques, including nonlinear effects such as plasticity and damage. Collectively, these reviews underscore the evolving nature of topology optimization and its expanding scope across various engineering domains.

Searching for design optimization problems with design-dependent pressure loads, boundary layers, or coated structures in the Scopus database, we can see the growth of these *boundary-effect-dominated* problems within the broader context of design optimization. That is, the data represent a wide range of methodological approaches, such as material distribution (density-based) topology optimization, level-set formulations, and classical shape and sizing optimization. Fig. 1 shows the expansion of this field in the past 20 years in terms of publications per year. Because the search spans a wide definition of design optimization, early contributions may be dominated by approaches other than material distribution methods. In other words, the figure illustrates the growing interest in boundary-effect-dominated problems within design optimization generally.

In line with this trend, we present a review of material distribution methods for *boundary-effect-dominated* problems. These problems involve significant effects associated with the boundary of the design, which add complexity compared to the interior regions. To solve these problems, the boundary must be identified as part of the optimization. The performance and the optimization outcome are heavily influenced by the behavior at the design boundaries. From an optimization perspective, boundaries are more difficult to handle as part of material distribution-based optimization compared to approaches that work directly on the boundary, such as level-set methods. In this review, we limit our attention to material distribution-based methods.

## 2 History of related ideas

The classical material distribution method can be viewed as an instance of a broad class of methods in which a body occupying a domain  $\Omega_b$  with a complicated boundary shape—the material region in the case of the material distribution method—is embedded in a simple “hold-all” region  $\Omega$ , typically equipped with a Cartesian mesh (Fig. 2). Depending on the application, the problem of interest can either be set in  $\Omega_b$  or in  $\Omega \setminus \Omega_b$ . This is an old idea; Hyman (1952, § 23) suggested one such method already in the early dawn of computing. Over the years, such methods have been given various epithets such as *fictitious domain*, *domain embedding*, or *immersed boundary* methods. Methods of this kind provide a mechanism so that the correct boundary conditions at  $\partial\Omega_b$  are satisfied exactly or approximately, although  $\partial\Omega_b$  is interior to  $\Omega$ . Here, we give a short overview of a selection of such methods in light of design optimization and, in particular, the material distribution method.

Various motivations for the use of embedding methods have been given:

- The numerical method of interest is fundamentally Cartesian, such as the finite difference or spectral method, and therefore nontrivial to adapt to complicated boundary shapes.
- Cartesian meshes on squares or cubes are beneficial in the context of fast solvers.
- Sometimes the shape of  $\Omega_b$  is so complicated, for example, a full car, that the generation of even unstructured body-fitted meshes can be too cumbersome and time-consuming to apply.
- The domain shape itself is an unknown, such as in fluid–structure interaction or design optimization.

The label *immersed boundary method* was introduced by Peskin (1972) within the Computational Fluid Dynamics (CFD) community, and these methods have seen explosive growth during the past 25 years, as analyzed by Verzicco (2023) in a recent review. In CFD applications, the fluid flow

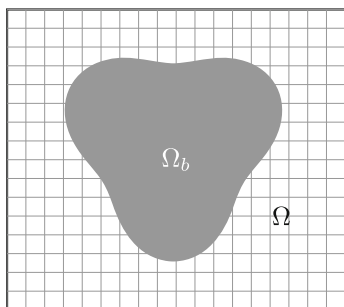


**Fig. 2** In a fictitious-domain method, a body  $\Omega_b$  is embedded in a hold-all region  $\Omega$  with a simple shape

is in  $\Omega \setminus \Omega_b$ , and the immersed boundary method is mainly used to set no-slip wall conditions on  $\partial\Omega_b$ , that is, vanishing Dirichlet boundary conditions for the velocity field; only a very limited number of studies have explored other types of boundary conditions. Most methods exploit that the Navier–Stokes equations express the balance of momentum to add an artificial forcing term to the strong form of the equations in order to impose the no-slip condition. Not all of the proposed methods are directly applicable in the context of gradient-based design optimization, since it may be difficult to effectuate smooth shape changes of  $\partial\Omega_b$  with respect to a set of design variables.

The label *fictitious-domain method* was introduced in the Russian literature already in the 1960s (Saul’ev 1963). Compared to the typical immersed boundary method, a more mathematical approach is typically taken by the authors who use the label fictitious domain or domain embedding methods, for instance by attempting to establish rigorous error estimates. Fictitious domain methods were, at least initially, developed for second-order elliptic problems such as the Poisson equation, the Helmholtz equation, and the equations of linear elasticity set in  $\Omega_b$ . In this approach, the boundary conditions on  $\partial\Omega_b$  are regarded as *constraints* on the problem set in  $\Omega$ . Such a constraint can be added as an extra equation defined either on  $\partial\Omega_b$  or  $\Omega \setminus \Omega_b$ . This constraint can then be enforced by adding an extra field variable, a Lagrange multiplier, to the elliptic equation. Alternatively, the constraint can be enforced or approximated by a penalty, avoiding the extra equation and the Lagrange multiplier.

There are various ways to carry out this method in practice. For Dirichlet boundary conditions imposed on elliptic problems, explicit use of Lagrange multipliers on  $\partial\Omega_b$  was used by Glowinski et al. (1994), and on  $\Omega \setminus \Omega_b$  by Glowinski and Kuznetsov (2007). An alternative to the use of Lagrange multipliers is to impose the Dirichlet condition using Nitsche’s method (Burman and Hansbo 2011), which is a consistent penalty method with optimal accuracy, avoiding both extra variables and the saddle-point problem. There is presently substantial interest in these methods (Burman et al. 2015), and these methods have been successfully used for shape optimization (Bernland et al. 2018; Burman et al. 2018).

There are also simpler types of penalty methods to enforce Dirichlet conditions, methods that often can be given a physical interpretation. For instance, the equation  $-k^2 E - \Delta E + i\alpha E = 0$  governs the amplitude of 2D transverse electric waves with wavenumber  $k$ . The parameter  $\alpha \geq 0$  is proportional to the electric conductivity of the medium. When  $\alpha = 0$ , the propagation is lossless, whereas  $\alpha > 0$  models the presence of Ohmic losses. Thus, wave propagation in  $\Omega \setminus \Omega_b$  in the presence of a perfect electric conductor in  $\Omega_b$  can be approximated with  $\alpha = 0$  in  $\Omega \setminus \Omega_b$  and  $\alpha \gg 1$  in  $\Omega_b$ . In this context,  $\alpha$  acts as a penalty parameter enforcing a vanishing Dirichlet boundary condition at  $\partial\Omega_b$ . The use

of a positive, finite value of  $\alpha$  leads to an approximation of a perfect electric conductor, an approximation that is well-motivated by the fact that real materials generally have a finite conductivity. For instance, this approach, generalized to the full 3D Maxwell equations in time domain, has been successfully used for material distribution topology optimization of metallic antennas (Hassan et al. 2014).

Another penalty approach for enforcing vanishing Dirichlet conditions is used for fluid flows. The system

$$\partial_t \mathbf{u} - \nu \Delta \mathbf{u} + (\mathbf{u} \cdot \nabla) \mathbf{u} + \nabla p + \alpha \mathbf{u} = \mathbf{0}, \quad (1a)$$

$$\nabla \cdot \mathbf{u} = 0 \quad (1b)$$

is the Navier–Stokes equations for the flow of an incompressible, viscous fluid with an added penalty term governed by the parameter  $\alpha \geq 0$ ;  $\mathbf{u}$  and  $p$  are the velocity and pressure fields, and  $\nu$  the kinematic viscosity. Fluid flow in  $\Omega \setminus \Omega_b$  with a no-slip boundary condition at  $\partial\Omega_b$  can be approximated by setting  $\alpha \gg 1$  in  $\Omega_b$  and  $\alpha = 0$  in  $\Omega \setminus \Omega_b$ . Note that the penalty effect is augmented by the incompressibility constraint (1b), which is also enforced in  $\Omega_b$ . A physical interpretation of system (1) is that it constitutes an interpolation between ordinary fluid flow in  $\Omega \setminus \Omega_b$  and Darcy flow in  $\Omega_b$ , that is, flow in a porous medium. The system is therefore sometimes labeled the Navier–Stokes/Darcy problem.

Material distribution topology optimization using the Stokes/Darcy problem (system (1) with  $(\partial_t + \mathbf{u} \cdot \nabla) \mathbf{u} = \mathbf{0}$ ) was introduced by Borrvall and Petersson (2003) and has been followed by many studies; Alexandersen and Andreasen (2020) reviewed the status of the field a few years ago.

In contrast to the Dirichlet case, it is much more straightforward to assign vanishing *Neumann* conditions for scalar second-order elliptic problems, or corresponding conditions for systems, such as *stress-free conditions* for linear elasticity or incompressible fluid flows. Assume that the problem of interest is set in  $\Omega_b$  with a Neumann-type condition at its boundary. After finite-element discretization, such a condition becomes incorporated in the variational formulation over  $\Omega_b$  as a “natural” boundary condition, so no additional mechanism, such as Lagrange multipliers or penalties, is needed to satisfy these boundary conditions. However, if the equations are to be solved in  $\Omega$ , some conditions have to be added to provide a well-defined solution in  $\Omega \setminus \Omega_b$ . The simplest approach is the one used in material distribution methods, where the variational form is extended by  $0 < \epsilon \ll 1$  into  $\Omega \setminus \Omega_b$ ; that is, the variational form will hold over the full domain  $\Omega$ , not only  $\Omega_b$ , but the contribution from the void region  $\Omega \setminus \Omega_b$  will be scaled down by  $\epsilon$ . Physically, for elasticity problems, this strategy corresponds to replacing void in  $\Omega \setminus \Omega_b$  with a low-density material. Thus, the classic material distribution topology optimization approach (Bendsøe 1989), at the center of this article, constitutes a fictitious-domain approach for the Neumann/stress-free problem.

To summarize: When representing a subdomain  $\Omega_b \subset \Omega$  using a distributed coefficient field, as in the material distribution method, homogeneous Neumann/stress-free boundary conditions as well as homogeneous Dirichlet conditions on  $\partial\Omega_b$  can be set using only the distributed field variable, without explicit tracking of  $\partial\Omega_b$ . Anything more complicated, such as Robin or impedance conditions or nonhomogeneous versions of the conditions, requires additional mechanisms, as will be reviewed in the following.

### 3 Design description and filtering

Filtering techniques are a cornerstone of material distribution topology optimization, serving multiple roles from regularization and length-scale control to the imposition of manufacturing constraints. In the context of boundary-effect-dominated problems, filtering plays a particularly important role by enabling the identification and manipulation of interfaces within the material distribution framework. This section reviews the principal filtering approaches relevant to boundary treatment. For further details, we refer interested readers to the review of density-based filtering and techniques for achieving length-scale control by Lazarov et al. (2016).

Throughout this section, we will refer to the unknown in the optimization problem as the design. From an analytical perspective, the design is a function  $\alpha$ . In numerical implementations, this function is represented by a vector  $\boldsymbol{\alpha}$ , which contains the decision variables in the optimization problem solved in practice. Over the decades, significant effort has gone into defining how a given design maps to the physical quantities of interest, such as density or conductivity. The most common choice is to have  $\alpha \in L^\infty(\Omega)$  such that  $0 \leq \alpha \leq 1$  almost everywhere. In a typical discretization, such as finite elements,  $\alpha$  is replaced by an element-wise constant function  $\alpha_h$ , whose element values are stored in  $\boldsymbol{\alpha}$ . A common alternative is a nodal-based description, where  $\alpha_h$  is determined by its nodal values, which are stored in  $\boldsymbol{\alpha}$ .

It was recognized early on that direct optimization over the coefficient field of the physical quantity of interest leads to robustness issues, such as checkerboarding and mesh dependency (Sigmund and Petersson 1998). Borrvall (2001) systematically investigated several techniques to resolve mesh dependency and ensure the existence of a solution to the minimum compliance problem.

To address challenges like checkerboarding and mesh dependency, filters similar to those used in image analysis have become widely adopted tools. The combination of filtering, penalties, and gradient-based optimization has been pivotal to the success of material distribution-based design optimization in general. Filters are also a key component in many of the methods dealing with boundary-dependent problems. These methods deserve special attention. In this

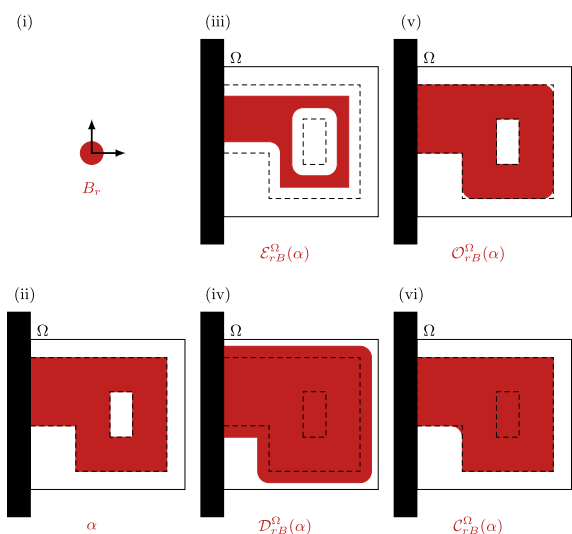


**Fig. 3** Morphological operators with structuring element  $B_r$  of radius  $r$  applied to a test design  $\alpha$  (ii), which is clamped to a wall (in black) on the left side of the design domain  $\Omega$ . The middle and right columns show the erode (iii), the dilate (iv), the open (v), and the close (vi) operators

section, we highlight the main ideas and a few representative contributions.

The earliest use of filtering in topology optimization targeted the sensitivities—the derivatives of the objective function (Sigmund 1994, 1997). Sensitivity filtering mitigated many of the numerical instabilities, such as checkerboarding. In 2001, Bruns and Tortorelli (2001) proposed a density filtering scheme in which the design itself was subject to filtering. The name density filtering reflects its historical roots in linear elasticity, where the physical quantity of interest was the material density. That same year, Bourdin (2001) established the existence of solutions to a density filtered version of the penalized minimum compliance problem.

Linear filtering smooths the design, counteracting the penalty by inducing areas of intermediate “densities.” As a result, the introduction of linear filtering was soon followed by a sequence of contributions exploring nonlinear alternatives. The first nonlinear filtering method was suggested by Yoon and Kim (2003), who introduced an S-shaped scaling function to drive intermediate densities toward 0 or 1. Subsequently, Guest et al. (2004) suggested using a linear filter followed by the element-wise application of a nonlinear activation function. Building on this idea, various nonlinear activation functions have been proposed. Today, the most widely used approach is a tanh-based approximation of a shifted Heaviside function, as proposed by Wang et al. (2011).

The design in topology optimization is typically represented as a discretized field on a structured mesh—just like a digital image. This similarity motivates the use and adaptation of tools from image processing, such as mathematical morphology—a framework developed for image analysis and

the manipulation of geometric structures. Heijmans (1995) provides a concise introduction to this field. Generally, morphological operators are defined on  $\mathbb{R}^n$ . However, in topology optimization, the design domain is a bounded subset of  $\mathbb{R}^n$ . As a result, special care is needed when applying filters near the boundary of the design domain. Figure 3 illustrates the effect of various morphological operations on a test design  $\alpha$  (ii) within the design domain  $\Omega$ . The material is clamped to a fixed wall (in black) on the left, outside the design domain. The figure shows, column by column, the effects of the erode (iii), the dilate (iv), the open (v), and the close (vi) morphological operators using the structuring element  $B_r$  (i) on a given design (ii).

In 2007, Sigmund (2007) introduced nonlinear filters that mimic morphological operators using the Kreisselmeier–Steinhauser (KS) approximations (Kreisselmeier and Steinhauser 1983), which approximate the min and max operators in terms of exponential functions. Soon after, combinations of morphology-inspired filtering and nonlinear activation strategies were suggested by Sigmund (2009) and Guest (2009). Svanberg and Svärd (2013) extended Sigmund’s (2007) morphology-mimicking filters using continuous approximations of the min and max operators based on Pythagorean means. Wadbro and Hägg (2015) introduced the class of  $fW$ -means, which provides a general framework that includes all the above filters and enables further generalization. In short, this framework includes all filters that can be written in the form

$$\mathcal{F}(\alpha)(x) = g \left( \int \Phi(x, y) f(\alpha(y)) dy \right), \tag{2}$$

where  $\Phi(x, y) \geq 0$  is a filter kernel such that  $\int \Phi(x, y) dy = 1$  for all  $x$ , and  $f$  and  $g$  are smooth invertible functions such that  $g \circ f : [0, 1] \mapsto [0, 1]$ . In a follow-up study, Hägg and Wadbro (2017) extended Bourdin’s (2001) existence result for the minimum compliance problem to cascades of generalized  $fW$ -mean filters. In this setting, for each  $x$ , the kernel  $\Phi(x, y)$  has support in a neighborhood  $\mathcal{N}_x$  of strictly positive size.

Traditionally, filters use convolution-type kernels,  $\Phi(x, y) = \varphi(|x - y|)$ , where  $\varphi$  has compact support. For large-scale problems on non-uniform meshes, an attractive alternative is to perform filtering via the solution of a partial differential equation for which fast solvers exist. The most common approach is to define a linearly filtered version  $\mathcal{L}$  of a field  $\ell$  as the solution to the strongly elliptic equation

$$-r^2 \nabla \cdot \nabla \mathcal{L} + \mathcal{L} = \ell, \tag{3}$$

where  $r > 0$  is a parameter. PDE-based filtering was first introduced as a sensitivity filter at the 8th WCSMO in Lisbon (Lazarov and Sigmund 2009) and was soon thereafter

extended to density filtering (Kawamoto et al. 2011; Lazarov and Sigmund 2011). This approach also fits into the  $fW$ -filter framework, with  $\Phi(x, y)$  being the Green’s function for the boundary value problem (3). The vanilla version of the PDE filter uses  $f = g = \text{id}$ , the identity function, in definition (2). Nonlinear functions  $f$  and  $g$  can also be applied pointwise (or element-wise after discretization) to enhance the flexibility of the PDE-based filter. Currently, the most common approach uses  $f = \text{id}$  and  $g$  as a tanh-based approximation of the Heaviside function.

The above discussion has focused on filtering in general. In practice, the design domain  $\Omega$  is bounded, which needs to be taken into account when defining the filtering operators. In convolution-based filtering, this is typically handled by padding the design or by appropriately redefining the filtering operators (Bruns and Tortorelli 2001; Wadbro and Berggren 2006; Lazarov et al. 2016; Clausen and Andreassen 2017; Hägg and Wadbro 2018). For PDE-based filtering, the fact that  $\Omega$  is bounded is treated by imposing proper boundary conditions to achieve an appropriate behavior of the filtered field near the boundaries of  $\Omega$  (Lazarov and Sigmund 2011; Wallin et al. 2020).

### 3.1 Computational complexity and versatility

Traditional filtering using convolution-type kernels with compact support and PDE-based filtering should not be seen as competing approaches. Each method offers distinct advantages. Convolution-based filters provide detailed and explicit control over the smoothness of the design. For structured meshes, convolution-based filters are straightforward to implement and computationally efficient. In contrast, PDE-based filters are also well suited for complex geometries and can leverage highly optimized PDE solvers, making them practical for solving large-scale problems in parallel computing environments. Although PDE-based filters do not explicitly control the feature size, the parameter  $r$  in partial differential equation (3) is closely correlated with the filtered design’s minimum feature size (Lazarov and Sigmund 2011).

### 3.2 Cascades of filters and multi-field representations

A key component for the successful application of material distribution topology optimization methods for boundary-effect-dominated problems is the use of cascades of filters, multi-field design representations, or a combination of the two. The structure of the basic cascaded filter operator in the discretized case is:

$$\begin{aligned} & \mathcal{F}_n \circ \mathcal{F}_{n-1} \circ \dots \circ \mathcal{F}_1(\alpha) \\ &= \sigma_{n+1} \left( \mathbf{W}_n \sigma_n \left( \dots \mathbf{W}_2 \sigma_2 \left( \mathbf{W}_1 \sigma_1 (\mathbf{I} \alpha) \right) \right) \right), \end{aligned} \tag{4}$$

where  $\sigma_1 = f_1$ ,  $\sigma_k = f_{k+1} \circ g_k$  for  $k = 2, 3, \dots, n$ , and  $\sigma_{n+1} = g_n$ , in which  $f_k$  and  $g_k$  are the nonlinear functions in the  $k$ th filter, and  $\mathbf{W}_k$  is a matrix encoding the linear averaging performed by the  $k$ th filter in the sequence, and  $\mathbf{I}$  is the identity matrix. This defines a sequence of element-wise applications of activation functions  $\sigma_k$  and matrix–vector products, which mirrors the structure of a basic neural network. Thus, this cascade of filter operations can be interpreted as a pre-trained network whose task is to map the design vector  $\alpha$  to a physical design with desired properties—most commonly, a minimal feature size. Generalizations of this framework—such as multi-field input and output representations—can also be viewed as pre-trained networks that enable the definition of additional features, such as the area of infill and coating.

An additional advantage of cascaded filters is their ability to identify or recover the design interface—an essential feature in boundary-effect-dominated problems, where precise interface characterization is critical. By carefully designing the structure and parameters of the cascade, one can extract a boundary strip without explicitly tracking the interface. Section 6 reviews several strategies for achieving this, focusing on filter-based interface identification methods.

## 4 Design-dependent pressure load

Designing structures subject to design-dependent loads—such as pressure loads applied on the structural surface—is quite challenging within the standard topology optimization framework. These problems typically involve the steady-state equations of linear elasticity for a body  $\Omega_b \subset \mathbb{R}^d$ , augmented by a pressure load  $p$  acting on parts of the design surface  $\Gamma_p \subset \partial\Omega_b$ , with variable position, direction, and magnitude. Figure 4 illustrates the domain  $\Omega_b$ . Thus, the displacement  $u$  of the structure is the solution to

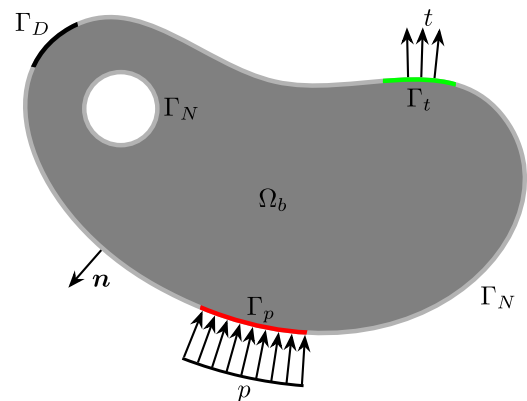


Fig. 4 Arbitrary design domain  $\Omega_b$  for a design-dependent pressure load problem

$$-\nabla \cdot \sigma(u) = f \quad \text{in } \Omega_b, \tag{5a}$$

$$u = u^* \quad \text{on } \Gamma_D, \tag{5b}$$

$$\mathbf{n} \cdot \sigma(u) = t \quad \text{on } \Gamma_t, \tag{5c}$$

$$\mathbf{n} \cdot \sigma(u) = p \quad \text{on } \Gamma_p, \tag{5d}$$

where  $f$  is the body force,  $u^*$  is a prescribed displacement along  $\Gamma_D \subset \partial\Omega_b$ ,  $t$  is the boundary traction on  $\Gamma_t \subset \partial\Omega_b$ , and  $\mathbf{n}$  is an outward-pointing normal vector.

For homogeneous and isotropic materials, the stress tensor  $\sigma(u)$  and the corresponding strain tensor  $\epsilon(u)$  are

$$\sigma(u) = E\epsilon(u) = 2G\epsilon(u) + \lambda\text{tr}(\epsilon(u))I, \tag{6}$$

$$\epsilon(u) = \frac{1}{2}(\nabla u + \nabla u^T), \tag{7}$$

where  $E$  is the fourth-order elasticity tensor,  $G$  is the shear modulus, and  $\lambda = K - (2/d)G$  is the dimension-dependent first Lamé parameter with bulk modulus  $K$ , and  $d = 2, 3$  for 2D and 3D problems, respectively. As the design evolves, the shape and location of  $\Gamma_p$  change, leading to a strong coupling between geometry and loading. This coupling highlights a fundamental limitation of traditional material distribution approaches, which typically do not explicitly identify or resolve boundary features. In the following, we review methodologies that have been developed to address this limitation, with a focus on problems involving design-dependent pressure loads.

### 4.1 Parameterized surface methods

The first material distribution topology optimization method addressing boundary-dependent load effects was introduced by Hammer and Olhoff at the 3rd World Congress on Structural and Multidisciplinary Optimization (Hammer and Olhoff 1999, 2000). This study aims to minimize the standard structural compliance with an additional pressure load  $p$  acting on parts of the design surface  $\Gamma_p$ . The pressure loading is applied using a parameterized isovolumetric density surface, inspired by the isoline-based adaptive techniques of Maute and Ramm (1995) for identifying structural boundaries. More precisely, the pressure load surface  $\Gamma_p$  is controlled by the distribution of design variables, where the nodal density distributions  $\bar{\alpha}_i$  are the mean densities of all elements that share the node  $i$ . An interpolation is then constructed from these node values  $\bar{\alpha} := (\bar{\alpha}_i)_{i=1}^M$  to obtain a set of points  $\mathbf{x}_f = \{\mathbf{x}_f\}$ , where the interpolated densities at these points are equal to a prescribed value for a surface of isovolumetric density,  $\alpha_c$ . By choosing  $\alpha_c$  carefully, the surface is forced to lie strictly inside the structural domain. Then, fitted Bézier curves, whose control points  $\mathbf{x}_c = \{\mathbf{x}_c\}$  are determined by  $\mathbf{x}_f$ , are constructed. Hence, a smooth surface extracted from

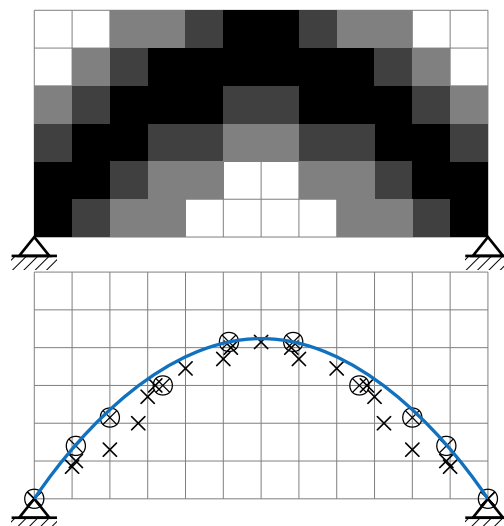


**Fig. 5** Illustration of a load-carrying surface interpolation and reconstruction based on non-uniform density distribution. Top: Two-dimensional design with non-uniform and discrete material distribution. Bottom: points of equal density  $\mathbf{x}_f$  (x) and the fitted Bézier curves (blue) and their control points  $\mathbf{x}_c$  (⊗). Adapted from Hammer and Olhoff (2000)

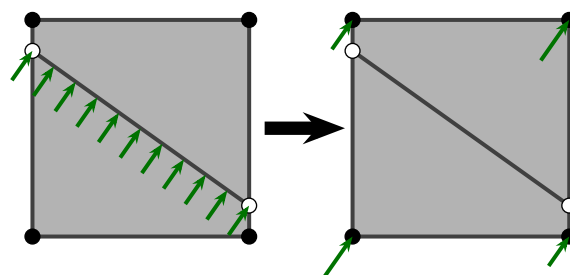


**Fig. 6** Demonstration of the nodal force calculation. Left: Pressure load acting on a straight line that approximates a segment of a smooth surface within an FE element, right: Corresponding equivalent nodal forces of an FE element

those curves is used as the structural loading surface as shown in Fig. 5.

Each segment of this smooth surface that intersects an FE element is approximated by a straight line as part of approximating the pressure load. The nodal forces are computed by integrating the product of the basis function and the pressure load along this segment. Finally, the load on an FE element is distributed to all its nodes, so the load is dispersed as illustrated in Fig. 6.

On the one hand, this method keeps the FE mesh fixed, avoiding the complexity of varying domain shapes, and benefits the sensitivity analysis by mitigating the non-differentiability caused by possible coincidences between the loading surface and element boundaries. On the other hand, the sensitivity of the pressure load with respect to the variations in element density must be ascertained through the relationship between the isovolumetric density and the

spline function control points, which complicates the analysis. However, the isoline may not always successfully identify the valid loading surface, because the cut-off value  $\alpha_c$  is selected based on experience. Despite the persistence of certain difficulties, Hammer and Olhoff (2000) provides an overview of pressure load problems and opens a new research topic within topology optimization, namely boundary-effect-dominated problems.

Later, Du and Olhoff (2004a, b) proposed an approach to identify the loading surface in two consecutive papers (for 2D and 3D, respectively) based on the isoline technique originally proposed by Maute and Ramm (1995). They used a modified isoline strategy that incorporates material density information from both the current and previous iterations. This enhancement yields a more stable and well-defined representation of the pressure surface  $\Gamma_p$ , while also enabling a straightforward implementation. Unlike Hammer and Olhoff (2000), in this method, the contour level  $\alpha_c$  is dynamically varied during optimization. To prevent isoline discontinuities, or so-called iso-parametric islands, the method imposes an angle constraint: the angle  $\theta$  between the new and old boundary segments is constrained by  $|\theta| \leq \theta_c$ , ensuring a smooth evolution of the pressure boundary. If no new segment meets this condition, the isoline level is adaptively adjusted to identify a valid loading surface; otherwise, the loading surface from the previous iteration is reused. The proposed modifications overcome the limitations of the previous method by Hammer and Olhoff (2000) and eliminate the iso-parametric island issue. However, this method still requires predefined isoline endpoints, which may prevent the actual design from being fully included in the discretized domain, especially when no symmetry line intersects the structure.

Fuchs and Shemesh (2004) proposed another material distribution-based method to identify the loading surface, referred to as the parametric loading surface. Although similar to the method by Hammer and Olhoff (2000) in its use of Bézier splines, this method employs high-order Bézier-spline control points independent of the design variables to represent the loading surface. More precisely, the  $x_1$  coordinates of the control points are fixed and evenly distributed along the  $x_1$ -axis, while the  $x_2$  coordinates are treated as additional design variables, independent of the density field  $\alpha$ , as shown in Fig. 7. To prevent rigid-body translation of the structure within the design domain, one control point—represented by a black dot in Fig. 7—is deliberately held fixed throughout the process.

Hence, the pressure load is applied to that surface independently of the material distribution. To avoid numerical instabilities caused by sharp transitions between solid and void material, Fuchs and Shemesh (2004) also introduced the so-called transition zone in a neighborhood of the fluid–solid interface, where the elasticity increases gradually from void to solid. Finally, this method is used to solve the com-

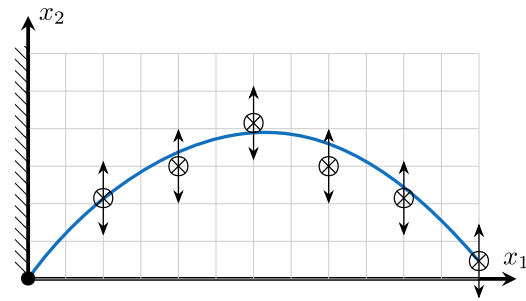


**Fig. 7** Demonstration of parametric loading surface with control points ( $\otimes$ ) and a fixed point ( $\bullet$ )

pliance minimization topology optimization with respect to not only  $\alpha$  but also the  $x_2$ -coordinates of the control points. Although the approach is similar to earlier works (Hammer and Olhoff 2000; Du and Olhoff 2004a, b), this method uses the independent pressure surface in conjunction with the weak material zone to generate a smooth solid–void interface. Notwithstanding, the introduction of an independent pressure boundary and additional design variables increases the complexity of an already challenging optimization problem.

To address the limitations of the method by Du and Olhoff (2004a, b), Lee and Martins (2012) proposed a method for identifying the loading boundary using directional nodal-based iso-density that connects points of equal material density within the design domain. This approach avoids the dependence on the previous iteration's isoline by assuming that changes in material distribution between steps are small. Instead of updating the isoline incrementally, this method constructs the isoline from scratch at each iteration by prescribing the void area. Specifically, the nodal relative densities are defined either by interpolating over surrounding elements, for element-based design frameworks, or directly in nodal-based schemes. A set of points  $x_f$  is then constructed by linear interpolation from nodal relative densities with a prescribed contour level  $\alpha_c$  following the approach by Hammer and Olhoff (2000). However, rather than using a fixed  $\alpha_c$ , this method starts with a small value and increases it progressively as the topology evolves and becomes more defined. The first point of the isoline loading boundary is selected from  $x_f$  based on the center of the predefined void area. If the center does not lie on an element boundary, a small local arc search is performed to locate the nearest valid point. Subsequent points are traced sequentially in a specified direction (clockwise or counterclockwise), selecting at each step the candidate point that minimizes the angle change to maintain a smooth path. Once the isoline is fully constructed, the surface pressure load is distributed to the equivalent FE-nodal loads as shown in Fig. 6. This method resolves most of the challenges with spline- and isoline-based approaches. Although using analytical sensitivities reduces the compu-

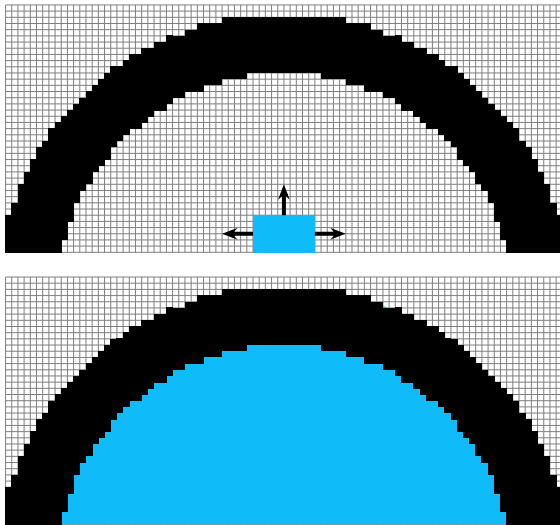


**Fig. 8** Demonstration of the design domain before (top) and after (bottom) propagation process of the “fluid flooding” boundary tracking method

tation cost compared to finite differences, determining the isoline from scratch at each iteration, as done in this method, still introduces considerable complexity in both implementation and computation.

## 4.2 Material phase-based methods

Shortly after the first material distribution optimization formulation for design-dependent pressure load problems by Hammer and Olhoff (2000), Chen and Kikuchi (2001) used a similar system as the one in equation (5) to minimize the total potential energy of the structure. However, instead of explicitly constructing a parameterized surface for the pressure load, they simulated the design-dependent load within the classical topology optimization procedure by using fictitious thermal loads. The problem is reformulated as an optimal distribution of the solid, void, and hydrostatic fluid phases within the design domain. The hydrostatic pressure force acting on  $\Gamma_p$  is approximated using a so-called pseudo-linear form, defined as the difference between the thermal load and the virtual work done by the forces acting on the prescribed (or free) boundaries of the fluid and solid regions. A so-called fluid flooding method is then used to track the fluid and solid interfaces. A fixed fluid region is always included in the initial design, which is then propagated to its adjacent void elements until those adjacent void regions are filled with liquid material as demonstrated in Fig. 8. Thus, a structural boundary is determined.

The pseudo-load vector can be computed via a finite-element analysis of a homogeneous solid subject to a fixed temperature change under free expansion. Furthermore, this approach can be used to simulate not only the

hydrostatic pressure loads but also the unidirectional loading. The pseudo-linear form enables natural integration of design-dependent loading into standard topology optimization, resulting in a method that is both straightforward to implement and computationally efficient. This concept is later extended to level-set topology optimization by Picelli et al. (2019); Lu and Tong (2021).

Bourdin and Chambolle (2003) presented a method for designing the stiffest structure subject to pressure loads or internal forces. The design domain is partitioned into three regions: solid, void, and a fictitious fluid that exerts pressure on the solid–fluid interface. A phase-field model incorporating a function  $\phi$  is used together with material interpolation schemes to ensure a smooth transition between different regions. The optimization objective is to minimize the compliance, defined as the total work of the pressure and internal forces at equilibrium. A penalization on the perimeter of the solid is applied to regularize the problem. The authors also analyze the model in the sharp-interface limit as the phase-field regularization parameter tends to zero.

A few years later, Clausen and Sigmund (2006); Sigmund and Clausen (2007) introduced a new approach to solve the pressure load problem based on a mixed displacement–pressure (incompressible) formulation, while remaining within the standard material distribution-based topology optimization framework. The key idea is to define the void region, where the pressure load occurs, as an incompressible, hydrostatic fluid, allowing pressure to be transferred through it. This is achieved by extending the classic topology optimization formulation to include pressure as a separate variable rather than relying solely on the typical steady-state equations. As a result, the void material is replaced by an incompressible fluid, enabling pressure transfer from external boundaries to the structure, regardless of its shape or topology. Specifically, the pure displacement formulation can be reformulated as the steady-state problem in mixed form by introducing a pressure variable defined by

$$p = -K \operatorname{tr}(\epsilon(u)). \quad (8)$$

Accordingly, substituting pressure expression (8) into definition (6) yields the constitutive law in mixed form for the stress tensor  $\sigma(u, p)$ . With this, the pressure boundary condition (5d) on  $\Gamma_p$  can be replaced by equation (8) throughout  $\Omega_b$ . Therefore, the governing equations (5) are reformulated in mixed form. The topology optimization problem is then solved using a three-phase material interpolation scheme, eliminating the need to define the pressure load boundaries. Although the mixed formulation introduces significantly higher computational costs than the standard formulation, it integrates directly with existing finite-element solvers, for example, the one implemented by Sigmund and Clausen using COMSOL. This compatibility makes it well suited for

standard material distribution-based approaches and enables extension to dynamic problems.

In the early 2020s, Kumar et al. (2020); Kumar and Langelaar (2021) introduced a new approach to optimize both elastic structures and compliant mechanisms subject to design-dependent pressure loads within the standard material distribution-based topology optimization scheme in 2D and 3D, respectively. Darcy's law, combined with a drainage term, models the design as a porous material, transferring design-dependent pressure loads into an equivalent body force. Darcy's law states that the apparent velocity  $\mathbf{q}$  is proportional to the pressure gradient. That is,  $\mathbf{q} = K(\alpha)\nabla p$ , where  $K(\alpha)$ , called *flow coefficient* by the authors<sup>1</sup>, depends on the design variable  $\alpha$ . To restrict pressure to boundary elements, a "drainage term"  $Q_{\text{drain}}$  is introduced to drain the flow/pressure only within the pressure loading boundary layer, so that negligible flow/pressure acts on interior structural boundaries. These concepts yield the PDE

$$-\nabla \cdot (K(\alpha)\nabla p) = Q_{\text{drain}}(\alpha), \quad (9)$$

where  $K(\alpha) = k_v - (k_v - k_s)H(\alpha)$ ,  $Q_{\text{drain}}(\alpha) = -h_s H(\alpha)p$ , with  $H$  a smooth approximation of the Heaviside function. Here,  $k_v$  and  $k_s$  are the flow coefficients of void and solid, respectively, and  $h_s$  is the solid drainage coefficient. The pressure  $p$  is converted into a body force  $b$  within an infinitesimal volume element as  $b dV = -\nabla p dV$ . With this concept, the boundary-dependent pressure condition (5d) is integrated into equation (5a) by replacing its right-hand side by  $f - \nabla p$ , where  $p$  solves equation (9). Note that, in this study, the internal body force  $f$  is set to zero. Treating the boundary-dependent pressure load as a body force enables solving design-dependent problems using the standard topology optimization framework with minimal changes. Furthermore, Kumar (2023) also presented an educational paper detailing the implementation. By utilizing this method, Banh and Lee (2024) later provided a comprehensive solution for optimizing thermo-mechanical-pressure systems. However, a tuning of the approximate Heaviside function's parameters remains necessary to balance differentiability and decisiveness in defining the loading boundary.

### 4.3 Image-based boundary detection

Moving away from conventional methods, Picelli et al. (2015) introduced design-dependent fluid pressure loading for evolutionary methods, particularly for the bi-directional evolutionary structural optimization (BESO) method (Querin et al. 1998). That is, the design variables can be either zero or one, so they represent either void or solid, respectively. Building on the idea by Yang et al. (2005), the authors

replace some selected void areas with incompressible fluid, thereby, removing intermediate densities. This simplification removes the need for intricate procedures to identify the fluid–structure interface, as the fluid, solid, and void phases are clearly distinguished throughout the optimization. Moreover, the fluid–structure interface is easy to control by allowing new fluid elements to appear only adjacent to existing fluid elements. The authors also present a thorough sensitivity analysis to address various scenarios arising from swapping single solid and fluid elements. The applicability of the latter approach to different evolutionary methods is shown by Sivapuram and Picelli (2020), where the authors use the topology optimization of binary structures (TOBS) method to handle design-dependent thermal expansion and fluid pressure loads.

Continuing along the line of innovative methods, Wang et al. (2016) proposed a scheme for identifying the pressure loading surface using image processing techniques inspired by level-set methods. In this approach, the results of material distribution topology optimization are treated as grayscale images. To detect image edges, the authors used a modified version of the Distance Regularized Level Set Evolution (DRLSE) method by Li et al. (2010), where the zero-level contour of a level-set function serves as the smooth pressure boundary. This boundary is then discretized into segments connecting the intersection points between the zero-level contour and the finite-element edges. As in spline- and isoline-based methods, the boundary pressure load is converted into equivalent FE-nodal forces. This conversion happens on elements intersected by the loading boundary, as shown in Fig. 6. The authors showed that this method works well for certain problems. However, it seems to be difficult and costly to implement due to the equivalent nodal force interpolation and the sensitivities of pressure loads calculation using finite differences. Fortunately, the DRLSE implementation can be simplified significantly thanks to the available code provided by Li et al. (2010). Moreover, the sensitivity analysis of loads can be avoided by using their proposed optimization framework, which assumes that the pressure loads remain unchanged in the given steps.

Nearly two decades after the first study on topology optimization for pressure load problems, Li et al. (2018) proposed a method that combines digital image processing with regional contour tracking to identify the loading surface during the optimization process. In particular, this method uses a boundary chain code to identify and track object boundaries. Here, the first step is to identify a starting point on the boundary. A typical choice is made by scanning the image from the top left to the bottom right of the image and letting the first material point be the starting point. This starting point now acts as the central point. Each point, or pixel in this case, has eight neighbors, numbered from 0 to 7 counterclockwise, starting from the left. Among these, at least

<sup>1</sup> It is usually called *hydraulic conductivity* in Darcy flow.

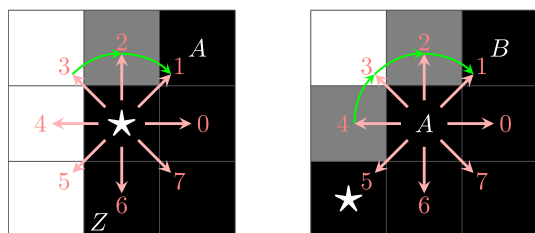
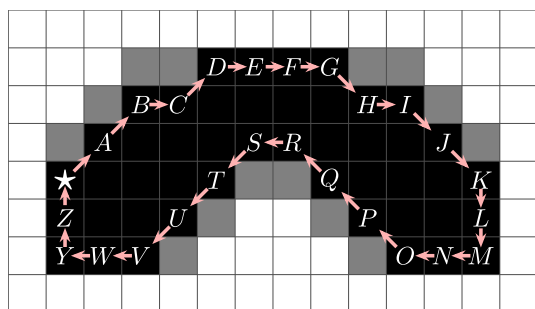


**Fig. 9** Pressure loading surface identification using regional contour tracking with boundary chain code. Top: Illustration of the boundary chain code, bottom left: boundary direction code for the starting point (★), bottom right: boundary direction code for the next central point (A)

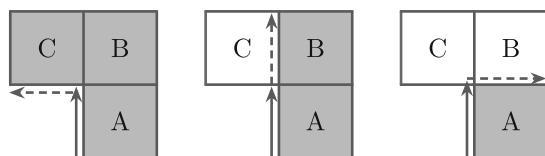


**Fig. 10** Demonstration of the identification of the upward-moving direction. Adapted from Zhang et al. (2008)

one must also lie on the boundary. To trace the contour, the algorithm selects the next point by searching clockwise until the first material neighbor is found, keeping the structure on the right side of the contour. The new point becomes the next central point. To avoid infinite loops, the starting search direction is chosen such that the previous central point is the last one to be checked. More precisely, it can be done by reversing from the previous search direction by 3 steps, i.e.,  $\text{mod}(\text{previous search direction} + 3, 8)$ , where  $\text{mod}(n, m)$  is the modulo operator that returns the remainder after integer division of  $n$  by  $m$ . Figure 9 illustrates the process. The starting point is marked (★) and its directions are shown in the bottom left panel. Since the starting point has no previous search direction, the algorithm begins at direction 3, selecting point A using direction 1. Now, A becomes the central point and its starting search direction is now 4 (chosen by reversing from direction 1 by 3 steps), then selecting B as the next central point via direction 1. The search ends when the next central point is the starting point or the prescribed endpoint.

Since the identified contour elements form a closed boundary of the structure, including other boundaries, the pressure

load boundary elements should be extracted from that based on the design specifications. The load sensitivities can be avoided, as the authors claim that the external load sensitivity is negligible. The advantage of this method is the ability to solve problems with not only external pressure but also internal pressure contained completely inside the design structure, which may be impossible for parameterized surface methods.

### 4.4 Element-wise boundary tracking

Due to the complexity of the previous methods, Zhang et al. (2008) proposed a simpler, element-based search scheme to identify pressure load surfaces for material-distribution-based topology optimization. The authors identify the load surfaces by connecting the boundary elements using vector lines along the elements' edges in four directions. This allows the pressure to act directly on the corresponding element nodes. To implement this scheme, a start and end point for the load curve are first selected. For simplicity, the points are chosen to have the structure lying on the right-hand side of the curve when following it from start to end. From the start point, the curve can proceed in one of four directions: upward, rightward, downward, or leftward.

Figure 10 shows an example of a boundary tracing proceeding upwards. In this case, there are three possible directions for the next step: leftward, upward, and rightward. If the next upward element C is solid, the path turns left. Otherwise, the new direction depends on the element B: if B is solid, the path continues upward; else B is void and the path turns right. The same logic applies to boundary tracing proceeding in other directions. Furthermore, the pressure is applied exactly to the element boundaries, so the sensitivities of the finite-element loads to the element densities can be neglected (Hammer and Olhoff 2000). Although this avoids the need for pressure sensitivity calculation, the method shares a limitation with the classic method by Hammer and Olhoff (2000): The selection of optimization parameters (e.g., predefined endpoints) is experience-dependent, and improper choices may cause invalid results.

In 2014, Lazarov et al. introduced the idea of using the spatial gradient of the density variable  $\alpha$  as boundary indicator, exploiting that the spatial gradient vanishes except on the solid-void interface. Based on this, Wang and Qian (2020) extended the concept to pressure load problems, especially when only portions of the boundary are subject to pressure loads. Using the gradient, the boundary load pressure is transferred into volume forces, as illustrated in Fig. 11. The authors apply only the pressure load on the outer boundary  $\Gamma_p$ , and keep  $\Gamma_0$  as a non-loading boundary. To do that, the approach introduces an auxiliary variable  $\alpha_{\text{aux}}$  that tracks the relevant interface parts during optimization. The update of auxiliary loading density is performed using a combination of PDE-based filtering and applications of a smoothed

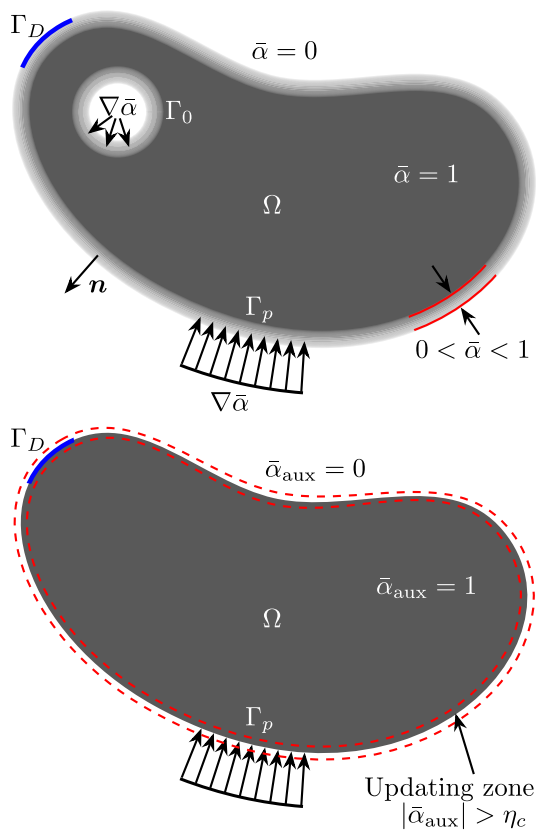


**Fig. 11** Comparison of the design-dependent loading on the entire solid–void boundary using physical density  $\bar{\alpha}$  and partial boundary interface using auxiliary density  $\bar{\alpha}_{aux}$ . Top: Physical density  $\bar{\alpha}$ , bottom: auxiliary density  $\bar{\alpha}_{aux}$ . Adapted from Wang and Qian (2020)

Heaviside function  $\hat{H}_{\eta_c, \beta_c}$ , with threshold  $\eta_c$  and sharpness control parameter  $\beta_c$ . The surface pressure load is translated to the volume force employing a boundary indicator  $|\nabla \bar{\alpha}_{aux}|$ , where  $\bar{\alpha}_{aux}$  is a standard approximate Heaviside mapping of  $\alpha_{aux}$ . As shown in Fig. 11,  $\bar{\alpha}_{aux} = 1$  inside the structure, the updating zone has  $|\bar{\alpha}_{aux}| > \eta_c$ , and zero elsewhere. When the pressure load is applied on the entire interface, the auxiliary density can be simply defined as  $\alpha_{aux} = \mathcal{F}(\alpha)$ , where  $\mathcal{F}$  is a PDE-based filtering operator. For partial interface loading, the authors compute the auxiliary density  $\alpha_{aux}$  by tracking the changes of  $\mathcal{F}(\alpha)$  near the loading boundary at each optimization step. Initially,  $\alpha_{aux}$  is set so that the pressure load is applied to the initial loading interface  $\Gamma_p$ . Successively, it is updated by tracking the changes of  $\mathcal{F}(\alpha)$  near the loading boundary within a selected updating zone, ensuring it remains unaffected by changes outside that zone. Finally, the updating zone is defined based on  $\nabla \mathcal{F}(\bar{\alpha}_{aux})$  and the auxiliary density  $\alpha_{aux}$  is updated through a density-gradient-based operator. The method supports local mesh refinement, enabling accurate identification of thin loading interfaces.

Shortly after Wang and Qian, Ibbadode et al. (2020) introduced the boundary identification and load evolution (BILE)

model to address design-dependent pressure load problems. To identify structural boundaries, the mean density value  $\bar{\alpha}_i$  at each node  $i$  is compared to a volume fraction threshold, which depends on the iteration number. The threshold typically increases monotonically during the optimization, reflecting the trend of the boundaries to become sharper as the optimization converges. To replicate this behavior, the method uses an exponential threshold function defined as

$$f_{th} = V \cdot \exp\left(\frac{k}{\mu} - 1\right), \tag{10}$$

where  $V$  is the volume fraction from the volume constraint of the optimization problem,  $k$  is the current iteration, and  $\mu$  is the threshold’s rate control factor. In two dimensions, a node  $i$  is considered a boundary node if its mean density  $\bar{\alpha}_i > f_{th}$  and it is shared by two elements holding a non-zero density value. However, during early iterations, many nodes satisfy these conditions, making boundary identification challenging. To address early-stage inaccuracies, the BILE method also takes into account the neighboring nodes and their associated elements. For two-dimensional quadrilateral elements, let  $S_i = \{\bar{\alpha}_{i,j}\}_{j=1}^4$  denote the set of mean densities of the four nodes surrounding node  $i$ , with corresponding element densities  $\alpha_{i,j}$ . Then, node  $i$  is classified as a boundary node if at most two of its surrounding nodes satisfy  $\bar{\alpha}_{i,j} < f_{th}$ . However, some of these identified nodes may stay within the structure, preventing the boundary from being smooth. Hence, only the outer nodes are selected to construct the boundary. Once the boundary nodes are identified, the pressure loading surface is defined based on their translational distance from the initial load surface and the presence of other boundary nodes in between. The direction of the pressure load—orthogonal to the load boundary—is computed using the gradient of the two nearest nodes. According to the authors, neither the force magnitude nor the loading angle is directly dependent on the density of boundary elements. Therefore, the sensitivity analysis for the pressure load is neglected. As with other threshold-based methods, this method may suffer from inaccuracies in the load boundary determination due to the presence of intermediate density elements in the SIMP interpolation.

### 5 Design-dependent heat flux

Unlike design-dependent pressure loads, which primarily arise in linear elasticity, design-dependent thermal loads typically appear in two distinct types of problems.

The first example is the electro-thermal-compliant (ETC) microdevice, a micro-electromechanical system (MEMS), which relies on compliant mechanisms for actuation. In these devices, motion is achieved through deformation induced by

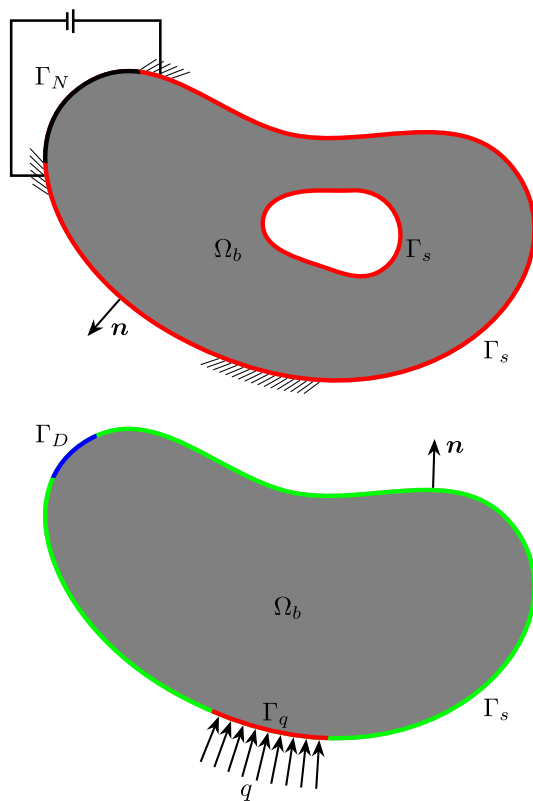


**Fig. 12** Arbitrary design domain  $\Omega_b$ . Top: for electro-thermal-compliant topology optimization, bottom: for design-dependent heat flux in thermal systems

electro-thermal Joule heating rather than rigid-body motion. The top panel of Fig. 12 demonstrates the general ETC problem, in which the body  $\Omega_b$  is subject to an electric current at two fixed locations. Hence, the electric current is distributed over the domain, which is therefore heated non-uniformly depending on its particular topology and shape. Thus, this electro-thermal Joule heating causes structural deformation, inducing a motion of the device.

If  $\Omega_b$  is a thin planar structure, heat can be expected to be convected away in the directions orthogonal to the plane. If  $\Omega_b$  is a 3D volume, heat will be convected away from its boundary. Therefore, thermal convection modeling, which is design-dependent, is essential for electro-thermally actuated devices.

The second class involves surface heat flux problems. These problems extend classical heat conduction by incorporating design-dependent thermal boundary conditions. As illustrated in the bottom panel of Fig. 12,  $\Omega_s$  holds a solid heat-conducting material subject to a prescribed temperature on  $\Gamma_D$ , a given incoming heat flux  $q$  through the boundary  $\Gamma_q$ , and heat dissipating through the design-dependent boundary  $\Gamma_s$ . Assuming that the surroundings are kept at a constant temperature, both cases use Newton’s law of cooling, which states that the heat loss rate is proportional to the tempera-

ture difference between the structure’s temperature  $T$  and its surroundings (the ambient temperature  $T_a$ ). More precisely, this approach approximates the interface heat flux along the design boundary  $\Gamma_s$  as

$$q_s(T) = h_c(T - T_a), \tag{11}$$

where  $h_c$  is the heat transfer coefficient. As with pressure loads, the challenge of determining the structural boundary often leads to neglecting the design-dependent effects of the heat transfer coefficient. In contrast to pressure load problems, where solutions like splines, reformulations, and image processing have been proposed, thermal load problems are typically tackled by interpolating the heat transfer coefficient from the structural boundary to the entire design domain. The standard form of this interpolation is

$$h_c(\alpha) = \gamma(\alpha)h_0, \tag{12}$$

where  $h_0$  is the base value of heat transfer coefficient, and  $\gamma$  is a structural boundary indicator function. Consequently, many studies aim to develop effective methods for determining the structural boundary indicator function  $\gamma$ .

Sigmund (2001a,b) was among the earliest to apply topology optimization to MEMS, considering the out-of-plane thermal convection effects, for one- and two-material structures, respectively. Although the work addressed design-independent heat transfer, it opened an important research direction for design-dependent thermal problems. One year later, Yin and Ananthasuresh (2002) proposed a method incorporating design-dependent thermal loads  $q_s$  into topology optimization for electro-thermal-compliant (ETC) microdevices, using two solid materials and void to enhance displacement. Instead of using the well-known SIMP-based material interpolation scheme for multiple materials introduced by Sigmund (2001b), the authors proposed representing each material by an interpolation based on a Gaussian distribution type “peak function,” avoiding the need for an extra fictitious density variable and its associated constraint for each material. The heat transfer coefficient  $h_c$  is then interpolated accordingly. More precisely, this interpolation takes the form (12) with the boundary indicator defined as

$$\gamma(\alpha) = \sum_{m=1}^{N_{\text{mat}}} e^{-(\alpha - \mu_m)^2 / 2\sigma_m^2} (1 - \alpha_N), \tag{13}$$

where  $m$  is the solid material index,  $N_{\text{mat}}$  is the number of solid materials,  $\alpha_N$  denotes the design density value of the neighboring elements, and  $\mu_m$  and  $\sigma_m$  are the mean and standard deviation of the Gaussian distribution function of the solid material  $m$ , respectively. Figure 13 illustrates the interpolation for two materials with different values for  $\sigma_1$  and  $\sigma_2$ .

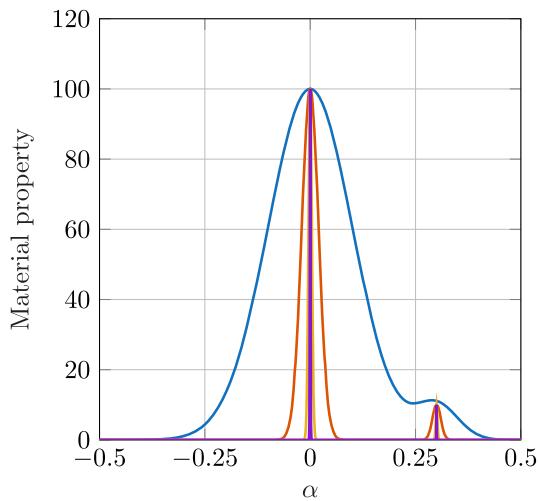


**Fig. 13** Two material ( $N_{\text{mat}} = 2$ ) interpolation curves using a single design variable:  $\mu_1 = 0$  and  $\mu_2 = 0.3$ . Adapted from Yin and Ananthasuresh (2002)

Thus,  $\mu_m$  represents the value of  $\alpha$  at which material  $m$  is exclusively selected, assuming  $\sigma_m$  is sufficiently small. In other words, the thermal load is applied to elements whose neighbors have zero interpolated material value. To ensure smooth material selection, the optimization begins with a large  $\sigma_m$ , which is gradually reduced to sharpen the peaks and yield physically meaningful results. Nevertheless, the choice of  $\mu_m$  and  $\sigma_m$  is essential, since inappropriate values may result in non-physical designs, such as those including free-floating or isolated material regions.

Boundary-dependent heat transfer was first introduced into reliability-based topology optimization (RBTO) of thermal systems by Moon et al. (2004). The key difference between reliability-based topology optimization and conventional topology optimization lies in the formulation of constraints. RBTO introduces probabilistic constraints to account for uncertainties in geometry and loading, even when the design variables are deterministic. In this model, the boundary indicator is

$$\gamma(\alpha) = (1 - \alpha^{1/p}), \tag{14}$$

where  $p > 1$  is a penalty parameter. This formulation approximates heat transfer at the design boundary using a planar heat transfer model. Thus, if  $\alpha = 1$ , then  $\gamma = 0$ , indicating that no heat transfer occurs inside the solid. Moreover, for  $\alpha = 0$ , this model assumes that the convection is unaffected by void regions. Under this interpolation, the heat transfer occurs primarily in the transition area ( $0 < \alpha < 1$ ), which typically corresponds to the design boundary. This model provides a simple yet effective extension of standard topology optimization to handle boundary-dominated heat transfer problems without introducing additional variables

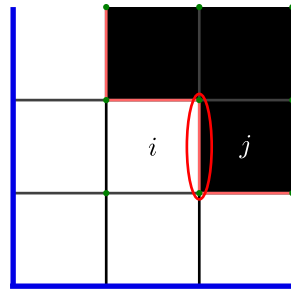
or parameters. However, since the method relies on material transition regions to define boundaries, it may fail to accurately capture sharp interfaces between solid and void.

In 2007, Bruns presented a comprehensive study on a “planar surface (design-independent) convection-dominated” problem and analyzed numerical instabilities. Although the work did not address shape dependencies, it introduced an idea and a potential solution to tackle material distribution topology optimization problems involving design-dependent heat transfer. In a different context, Yoon and Kim (2005) proposed a technique that controls structural topology by adjusting element connectivity rather than material density. Although this method does not target boundary effects, it introduces an alternative parameterization strategy that enables robust geometry handling. Soon after, Iga et al. (2009) introduced the homogeneous design method (HDM), a topology optimization approach for thermal problems dominated by boundary effects, considering shape-dependent heat transfer coefficients. Unlike conventional methods, HDM relaxes the design variable by introducing microstructures, modeling a two-scale composite material based on asymptotic homogenization. The method uses a hat function to identify the solid–void heat transfer interfaces that emerge in the fixed design domain, enabling proper application of heat transfer coefficients. The design boundary identification approach is similar to that of Moon et al. (2004), where intermediate density regions (grayscale areas) are interpreted as solid–void transitions. However, instead of the interpolation used by Moon et al. (2004), this study introduces a so-called smeared-out hat function as a boundary indicator. The smeared-out hat function acts as a boundary indicator function and is defined as

$$\gamma(\alpha) = \begin{cases} 0 & \alpha < \underline{\alpha} - \varepsilon, \\ \frac{1}{2} + \frac{\alpha - \underline{\alpha}}{2\varepsilon} + \frac{1}{2\pi} \sin\left\{\frac{\pi(\alpha - \underline{\alpha})}{\varepsilon}\right\} & \underline{\alpha} - \varepsilon < \alpha < \underline{\alpha} + \varepsilon, \\ 1 & \underline{\alpha} + \varepsilon < \alpha < \bar{\alpha} - \varepsilon, \\ \frac{1}{2} - \frac{\alpha - \bar{\alpha}}{2\varepsilon} - \frac{1}{2\pi} \sin\left\{\frac{\pi(\alpha - \bar{\alpha})}{\varepsilon}\right\} & \bar{\alpha} - \varepsilon < \alpha < \bar{\alpha} + \varepsilon, \\ 0 & \bar{\alpha} + \varepsilon < \alpha, \end{cases} \tag{15}$$

where  $\underline{\alpha}$  and  $\bar{\alpha}$  are, respectively, the lower and upper limit values for the extraction of boundaries for setting the heat transfer loads, and  $0 < \varepsilon \ll 1$  controls the numerical smearing bandwidth used in the hat function to avoid numerical singularities. In simple terms,  $\alpha < \underline{\alpha}$  corresponds to void,  $\bar{\alpha} < \alpha$  to solid, and  $\underline{\alpha} < \alpha < \bar{\alpha}$  to the structural boundary. The model also incorporates shape-dependent heat transfer coefficients  $h_0 = h_0(\alpha, p_f)$ , using a radial basis surrogate trained on simulations of sinusoidal fin structures. However, the surrogate model captures only local shape-dependent effects. As a result, this method may not accurately capture the heat transfer behavior for arbitrary geometries. Despite its improved boundary detection, the method may fail to cap-

**Fig. 14** An illustration for a solid–void interface (red) between element  $i$  and  $j$ . Blue lines denote the domain boundary, and gray lines are internal edges



ture sharp interfaces, as it defines boundaries through smooth transitions rather than discrete changes.

Following an idea suggested by Bruns (2007) and Alexandersen’s thesis work (2011), Zhou et al. (2016) published an industrial application of a topology optimization framework for a simplified steady-state heat transfer model with conduction and convection. In this framework, convection is modeled as an additional thermal flux, avoiding the need to solve the Navier–Stokes equations. The method employs a difference-based interpolation scheme, which evaluates the jump in design between adjacent finite elements, treating their common edge as part of the design boundary. For instance, for two neighboring elements  $i$  and  $j$  that share the same FE-edge, the boundary indicator can be computed by

$$\gamma_{c,i} = \frac{1}{2}g(\alpha_i - \alpha_j), \text{ and } \gamma_{c,j} = \frac{1}{2}g(\alpha_j - \alpha_i), \quad (16)$$

where  $g(\alpha) \approx |\alpha|$  to ensure that the boundary indicator is non-negative (Bruns 2007; Alexandersen 2011), and  $\gamma_{c,i}$  is the discretized boundary indicator used to determine the heat transfer coefficient contribution of element  $i$  to its shared edge with element  $j$ ; thus, each element contributes half of the convection to its shared interfaces (Fig. 14).

The total convection contribution is obtained by summing over each element in the FEM procedure. This study also provides an integrated Computer Aided Design (CAD) and Engineering (CAE) workflow for design optimization. Despite omitting some details for confidentiality, several industrial examples demonstrate the method’s applicability and practicality.

Nearly a decade later, Joo et al. (2017, 2018) proposed a surrogate modeling approach that accounts for variations in the heat transfer coefficient to optimize heat sinks under design-dependent cooling conditions in both two and three dimensions. This model improves upon that of Iga et al. (2009) by enabling the handling of arbitrary geometries. In particular, the heat transfer coefficients are computed using interpolation (12), where the boundary indicator  $\gamma$  is defined as

$$\gamma(\alpha_i) = \begin{cases} 1 & \text{if } \sum_{j \in \mathcal{N}_i} |\alpha_i - \alpha_j| \neq 0, \\ 0 & \text{otherwise,} \end{cases} \quad (17)$$

where  $\mathcal{N}_i$  denotes the set of indices of finite elements adjacent to element  $i$ . The shape-dependent variation of heat transfer coefficient  $h_0$  is approximated using the out-of-plane flow direction and the average heat transfer coefficient based on the Nusselt number correlation for plate-fin heat sinks proposed by Bar-Cohen and Rohsenow (1984). This approximation is based on the effective channel spacing  $w_{\text{eff}}$ , which depends on design density  $\alpha$ . At a design boundary element  $i$ , the effective channel spacing  $w_{\text{eff}}$  is defined as the minimum distance to another interfacial element  $k$  in the directions outward from the bulk solid structure. However, the use of a discrete boundary indicator function makes the problem non-differentiable. Using finite difference analysis, the authors showed numerically that the derivatives of boundary-dependent terms are negligible for small perturbations in the relative density.

In the previous section, the method proposed by Lazarov et al. (2014) and extended by Wang and Qian (2020), based on the observation that the spatial gradient of the design density is nearly zero throughout the design domain except at solid–void transitions, was applied to both design-dependent pressure and thermal load problems. In this work, the spatial gradient of auxiliary loading density  $\bar{\alpha}_{\text{aux}}$  acts as a boundary indicator function. More precisely, the boundary indicator is

$$\gamma = |\nabla \bar{\alpha}_{\text{aux}}|. \quad (18)$$

As previously mentioned, the auxiliary density is  $\alpha_{\text{aux}} = \mathcal{F}(\alpha)$ , where  $\mathcal{F}$  is a PDE-based filtering operator, since the design-dependent heat flux is applied on the entire boundary. Wang and Qian (2020) present a universal framework for topology optimization that can be applied to a wide range of problems in two and three dimensions. The numerical experiments were conducted using the open-source finite-element software FEniCS, facilitating straightforward replication. As with the methods by Moon et al. (2004); Iga et al. (2009), this method requires an adequate mesh resolution near the interface to ensure accurate evaluation of gradient-based loading heat transfer terms. To achieve a sharp boundary design, the authors employ a continuation strategy that gradually increases the steepness of the approximate Heaviside mapping during optimization.

## 6 Coated structures

When considering boundary-effect-dominated problems, coated structures may not come to mind immediately. Although coatings do not alter the boundary conditions or the governing equations themselves, a coating layer significantly influences overall system performance. In this sense, coated structures act as a bridge between bulk-dominated and boundary-dominated formulations: The different behavior of

the coating affects both the physics around the boundary of the design and the resulting optimized design. Thus, coatings introduce boundary-dependent effects, which place coated structures within the family of boundary-dominated problems.

Coated structures are appealing due to their versatility and the advantages they offer across a wide range of applications. When thoughtfully designed using a combination of different materials and structural patterns, coated structures can enhance performance, reduce cost, and improve manufacturability in many engineering applications. However, incorporating coated structures in the context of topology optimization is challenging, particularly when the goal is to optimize the coating and internal infill simultaneously.

The work by Guest (2009) is among the earliest contributions to topology optimization of coated structures—although this was not its original intent. The study aimed to develop a methodology for imposing minimum length scales on multiple phases in topology optimization problems. The method combined linear filtering with phase-specific radii, together with an approximation of the Heaviside function. A key feature is the independent scaling of each phase. Each phase is therefore assigned its own design variable field. The resulting distributions are then assembled to yield the final topology. To avoid overlap, the fields must be separated by a distance equal to the sum of their filter radii. This buffer zone at the interface between phases can effectively be interpreted as a coating layer. Although the author does not explicitly describe this region as such, the work lays the foundation for the subsequent development of topology optimization methods involving coated structures.

Although most techniques for coated structures have been developed within the context of compliance minimization, they vary significantly in their approaches and target applications. In this review, we consider two primary categories of coated structures: *shell-infill* and *substrate coating*. In the first category, a solid shell encloses a porous or lattice-based infill, often resulting in lightweight structures with tailored stiffness and strength. Some microscopic infills may also be optimized, leading to a multiscale design process. In the second category, a functional coating is applied to a solid substrate to enhance specific performance properties. Following the rapid growth of this field shown in Fig. 1, we chronologically explore various approaches to these problems—from early methods to recent developments—ranging from PDE filtering techniques to techniques based on mathematical morphology and image processing.

This section is organized as follows: in Sect. 6.1, we survey techniques employing the gradient of the design field; in Sect. 6.2, we explore the methods inspired by mathematical morphology; and in Sect. 6.3, the ones inspired by image analysis.

## 6.1 Gradient-based coating indicators

Following Guest (2009), Clausen et al. (2015) introduced one of the first techniques for the topology optimization of coated structures. The authors introduce a SIMP-based method for identifying the coating layer. This method uses a two-step filtering approach. First, a PDE filter  $\mathcal{F}_r(\alpha)$  with radius  $r$  smooths the design. Second, a scaling is applied using a tanh-based approximation of a shifted Heaviside function  $\mathcal{P}_{\beta,\eta}(\alpha)$ , where  $\beta$  controls the sharpness and  $\eta$  is the threshold value. The process consists of first computing the substrate, then identifying the coating layer. For the substrate  $\mathcal{S}$ , the design field is processed as

$$\mathcal{S}(\alpha) = \mathcal{P}_{\beta_1,\eta_1}(\mathcal{F}_{r_1}(\alpha)), \quad (19)$$

for some  $r_1$ ,  $\eta_1$ , and  $\beta_1$ . The next step is to compute the norm of the filtered design's gradient as

$$\|\nabla \mathcal{F}_{r_2}(\mathcal{S}(\alpha))\|_\varepsilon = \varepsilon \|\nabla \mathcal{F}_{r_2}(\mathcal{S}(\alpha))\|, \quad (20)$$

where  $r_2$  is a filter radius,  $\|\cdot\|$  denotes the Euclidean norm, and the normalization parameter  $\varepsilon$  is the inverse of the norm's maximum. The normalization ensures that the norm is compatible with the process, allowing the gradient norm to assume values between 0 and 1. Consequently, the coating layer is identified by scaling the normalized gradient of the filtered substrate. Namely, the coating is

$$\mathcal{B}(\alpha) = \mathcal{P}_{\beta_2,\eta_2}(\|\nabla \mathcal{F}_{r_2}(\mathcal{S}(\alpha))\|_\varepsilon), \quad (21)$$

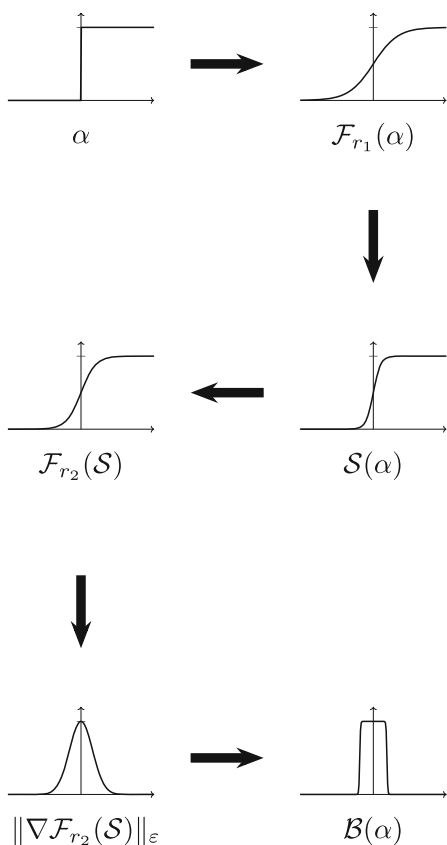
where  $r_2$ ,  $\eta_2$ , and  $\beta_2$  are parameters.

Figure 15 displays the workflow described above for identifying the boundary  $\mathcal{B}(\alpha)$  of a one-dimensional test-case design field  $\alpha$ . One benefit of the two-step approach is that it allows separate control of the length scales of the substrate and the coating using the respective radii  $r_1$  and  $r_2$ . To interpolate the substrate and the coating into the physical density  $P$  and the stiffness  $E$ , the authors modify the SIMP interpolation as follows:

$$\begin{aligned} P(\mathcal{S}, \mathcal{B}) &= \lambda_m \mathcal{S} + (1 - \lambda_m \mathcal{S}) \mathcal{B}, \text{ and} \\ E(\mathcal{S}, \mathcal{B}) &= E^0 (\lambda_E \mathcal{S}^p + (1 - \lambda_E \mathcal{S}^p) \mathcal{B}^p), \end{aligned} \quad (22)$$

where  $\lambda_m$ ,  $\lambda_E$ , and  $E^0$  are material parameters, and  $p$  is a penalization parameter.

The first application of the method proposed by Clausen et al. (2015)—targeting optimization under buckling loads—was presented by Clausen et al. (2016). In this application, the material is modeled as a solid shell with a triangular infill substrate to capture the characteristics of porous infills produced by additive manufacturing. Consequently, the authors consider the same material for both the coating and the



**Fig. 15** Two-step filtering workflow as described by Clausen et al. (2015). The normalized gradient of the processed one-dimensional test-case design  $\alpha$  is scaled to identify the coating layer  $\mathcal{B}(\alpha)$

substrate, using intermediate densities to describe the stiffness of the porous infill. Furthermore, Clausen et al. (2017) implemented and evaluated this shell-infill approach on 3D structural compliance cases. The numerical results show the method’s effectiveness in producing viable structures. Moreover, by using a void infill, the authors demonstrate the method’s applicability to shell-only design problems. For readers interested in optimizing the infill itself, we refer to Wu et al. (2018). There, the authors present a method to optimize the infill of a fixed shell using bone-inspired structures.

Based on the shell-infill approach, Wu et al. (2017) proposed a method for the concurrent optimization of a solid shell and a non-uniform porous infill. To achieve this, the authors introduced two different design fields:  $\alpha_s$  for the shell and  $\alpha_i$  for the infill. These two design fields are then processed through filtering and interpolation. Specifically, the shell is defined as  $\mathcal{B}(\alpha_s)$ , with  $\mathcal{B}$  defined in expression (21). To compute the porous infill, the substrate (19) derived from  $\alpha_s$  is multiplied by the processed infill design field  $\alpha_i$  as

$$\mathcal{S}(\alpha_i, \alpha_s) = \mathcal{P}_{\beta_1, \eta_1}(\mathcal{F}_{r_1}(\alpha_s))\mathcal{P}_{\beta_3, \eta_3}(\mathcal{F}_{r_3}(\alpha_i)), \tag{23}$$

for some  $r_3, \eta_3$ , and  $\beta_3$ . Moreover, to quantify the local material accumulation, an additional smoothing step is applied to the infill design field, as

$$\mathcal{F}_{r_4}(\mathcal{P}_{\beta_1, \eta_1}(\mathcal{F}_{r_1}(\alpha_i))), \tag{24}$$

for some radius  $r_4$ . The smoothed field is used to impose a local volume constraint, complementing the global volume constraint by limiting the maximum material accumulation per element. In this case, a robust formulation (Wang et al. 2011) is needed for both design fields to avoid degenerate designs where segments are partial shells with no infill. The design fields are then interpolated, including the multiple design fields, in a similar to that described in expressions (22). The presented numerical results show that the designs with non-uniform infill can outperform their counterparts with uniform infill. However, the use of two separate design fields, combined with a robust formulation, significantly increases the computational cost of calculating the sensitivities. Despite the associated computational overhead, Wang and Wu (2024) extended this approach to static and transient stress-constrained problems. Their simulations confirm the method’s effectiveness, while highlighting the substantial increase in computational effort as the design resolution increases.

To reduce the computational cost of high-resolution structures, several extensions of the two-step filtering scheme have been proposed. Building on the concept of non-uniform infill, Groen et al. (2019) proposed a method for coated structures with orthotropic infill. The filtering strategy is similar to the one introduced by Clausen et al. (2015). The novelty lies in the interpolation, which relies on a frame-shaped reference unit cell that can be elongated and rotated. The resulting microstructures are mapped onto a finer mesh (Groen and Sigmund 2018), enabling efficient modeling of high-resolution features. A key innovation of this method is that it avoids the need for a robust formulation, even for non-uniform infill. Instead, adaptive periodicity is used, along with enforced transition zones, to locally adjust the periodicity of the microstructure and prevent unsupported or “hanging” material at the microscale. Although effective, the method sometimes produces vanishing coating layers, which are restored during post-processing.

The work by Chu et al. (2019) is not explicitly aimed at optimizing coated structures. Nevertheless, it offers a concrete example of how the two-step filtering scheme can be extended, paving the way for future developments. The authors consider a multi-material problem and apply the gradient norm to identify the interface between the different material fields. The SIMP-based interpolation scheme is used to describe material properties and their graded interfaces.

Another application of the two-step filtering scheme that delves into material interface problems can be found in

the topology optimization of piezoelectric transducers. To avoid short-circuiting of the manufactured transducers’ components, a uniform null-polarity phase (gap-phase) of a few microns is required between areas of opposite polarity. Donoso and Sigmund (2016) employ a gradient-based coating indicator to model this gap-phase into the optimization process.

Building on the graded interface approach and drawing inspiration from bone-like structures, Dong et al. (2021) proposed a method to identify graded interfaces between the substrate and the coating layer. Their approach combines the two-step filtering strategy (Clausen et al. 2015) with the non-monotonic filter described by Chu et al. (2019), enabling the design of multi-gradient composites with several interface layers. In a follow-up study, Dong et al. (2025) applied this methodology to optimize the leading edge of aircraft wings. The resulting multilayer composites improve resistance to effects like bird strikes by mitigating damage and reducing structural deformation.

Motivated by the discrepancies between additively manufactured parts and their numerical counterparts, Xian et al. (2025) extended the two-step filtering method from Clausen et al. (2015) to include anisotropic materials. Such discrepancies are attributed to the specifics of the additive manufacturing process. In both polymer- and metal-based additive manufacturing, the mechanical properties of fabricated components are significantly influenced by process-dependent parameters such as the infill pattern and the cooling rate. To address this issue, the authors incorporated different directional tensile stiffnesses for the coating and the substrate into the material interpolation. For the simpler isotropic case, the authors also impose a local volume constraint, limiting the combined volume of coating and substrate in each subregion.

### 6.2 Morphology-inspired methods

Taking a step back in time, we find many other methods diverging from the gradient norm approach. One of the earliest such contributions is presented by Yoon and Yi (2019), who proposed a novel coating filter for coat–substrate structures, eliminating the need to compute the gradient of the design field. The study also investigates a key cause of why the coating layer may vanish under specific conditions. As a first step, a filter  $\mathcal{F}_r$  is applied to the design  $\alpha$ , using a specified radius  $r$ . The authors tested multiple filtering strategies, including a simple average, a weighted sum, and a  $p$ -norm density filter. Subsequently, the filtered design field goes through an S-shape function (Yoon and Kim 2003), which maps intermediate values closer to binary states (that is, 0 or 1). More precisely,

$$\mathcal{F}_{a,b}(\mathcal{F}_r(\alpha)) = \frac{1}{1 + \exp(a(\mathcal{F}_r(\alpha) - b))}, \tag{25}$$

where  $a$  and  $b$  are tuning parameters. Lastly, the outer coating layer is given by the product

$$\mathcal{B}_{\text{out}}(\alpha) = \mathcal{F}_{a,b}(\mathcal{F}_r(\alpha))(1 - \alpha). \tag{26}$$

The outer coating layer refers to the coating region outside the unprocessed design  $\alpha$ , which serves as the substrate. Conversely, to obtain the inner coating  $\mathcal{B}_{\text{in}}$ —that is, the region inside the design field  $\alpha$ —one can use the complementary field  $(1 - \alpha)$  as the starting design. Thus,

$$\mathcal{B}_{\text{in}}(\alpha) = \mathcal{F}_{a,b}(\mathcal{F}_r(1 - \alpha))\alpha. \tag{27}$$

The authors also illustrate how grayscale regions affect the resulting coating. Specifically, if the intermediate values are small enough, the coating layer does not appear. In numerical simulations, material properties are interpolated element-wise in the stiffness matrix using a SIMP-based approach. The mass constraint accounts for the combined mass of both substrate and coating. Some test cases exhibit the so-called *cheetah patterns*, meaning that the coating structure appears inside the substrate. These cheetah patterns can produce artificially enhanced stiffness, similar to the checkerboarding issue. To suppress these patterns, a penalization term or an additional constraint is needed.

Taking a different direction from the two-step filtering approaches, Luo et al. (2019) proposed an erosion-based approach for shell-infill structures. To compute the eroded design, the authors employ a PDE filter combined with a tanh-based approximation of a shifted Heaviside function, resulting in a formulation for the infill similar to the one for the substrate in (19). The eroded design  $\mathcal{S}(\alpha)$  is then subtracted from the initial design to obtain the shell structure. The choice of PDE-based filters over alternative filtering techniques is motivated by their capacity to handle large filter radii without significantly increasing the computational cost. To suppress checkerboard patterns and maintain a binary (black–white) design, the authors preprocess the design before the erosion step. The final expressions for the infill and the shell are given by

$$\begin{aligned} \mathcal{S}(\alpha) &= \mathcal{P}_{\beta_e, \eta_e}(\mathcal{F}_{r_e}(\mathcal{P}_{\beta_f, \eta_f}(\mathcal{F}_{r_f}(\alpha))))), \text{ and} \\ \mathcal{B}(\alpha) &= \mathcal{P}_{\beta_f, \eta_f}(\mathcal{F}_{r_f}(\alpha)) - \mathcal{S}(\alpha), \end{aligned} \tag{28}$$

for some preprocessing parameters  $\beta_f, \eta_f$ , and  $r_f$ , and for some erosion parameters  $\beta_e, \eta_e$ , and  $r_e$ . The material interpolation for the shell-infill structures follows the classical multi-material interpolation scheme (Bendsøe and Sigmund 1999). To avoid locally degenerate designs (only shell with no infill) and to ensure minimum length-scale control, the method uses a worst-case-based robust formulation (Wang et al. 2011). In this formulation, the mass constraint is applied to the dilated design, which is not updated at every iteration.

Instead, the intermediate design's mass fraction is updated every 20 iterations to reconcile the prescribed and current mass values. The study also provides a 1D analytical proof showing that the erosion operator achieves uniform corrosion depth over the whole structure. This highlights the method's ability to detect boundary interfaces, even for small features or large erosion radii. Their numerical results on 2D and 3D benchmark problems show the effectiveness of the proposed method. Nevertheless, in some extreme cases, thin branches with only shell structure were observed in the final design, lacking internal infill.

The work of Høghøj et al. (2020) shows the applicability of morphology-inspired methods outside the realm of coating layers. The authors, inspired by the work of Luo et al. (2019), employ an erosion–dilation approach to model a solid interface to provide strict separation between the two fluid phases of two fluid heat exchangers. This application shows the potential of the theory developed for coating structures in a multi-material interface case. Here, the erosion–dilation approach allows the authors to model three different phases, two liquid and one solid, using a single design variable. Moreover, the solid interface ensures strict separation between the two liquid phases, and the thickness of the solid phase can be controlled.

Extending the erosion-based approach, Wadbro and Niu (2019) propose an alternative to the use of PDE filters and Heaviside approximations. In this approach, the coating layer is identified through morphology-mimicking nonlinear filters (Hägg and Wadbro 2018). Particularly, they define  $\mathcal{E}_{rB}^\Omega(\alpha)$  and  $\mathcal{D}_{rB}^\Omega(\alpha)$  as the erode and dilate  $fW$ -mean filters, see equation (2), applied to the design field  $\alpha$  over  $\Omega$ , with radius  $r$  and structural element  $B$ . The coating layer is then identified as a strip of width  $r_c \in (0, r)$  along the boundary as described by

$$\mathcal{B}_{\{r,r_c\}rB}^\Omega(\alpha) = \mathcal{D}_{rB}^\Omega(\mathcal{E}_{rB}^\Omega(\alpha)) - \mathcal{D}_{\hat{r}B}^\Omega(\mathcal{E}_{rB}^\Omega(\alpha)), \quad (29)$$

where  $\hat{r} = r - r_c$ . The optimization is then performed simultaneously at both micro- and macroscales. Care must be taken when applying the filters near the design boundaries in both scales to avoid artifacts. Microscale properties are modeled using a SIMP approach. The effective properties of the periodic microstructures are interpolated using the novel implementation of asymptotic homogenization (Cai et al. 2014). Thus, the micro- and macroscopic properties are linked using the Porous Anisotropic Material with Penalization (PAMP) (Niu et al. 2009) method. Numerical experiments on standard structural compliance minimization suggest that coating thickness significantly affects both the microstructure infill and the overall macroscale design. Consequently, simultaneous optimization across scales may yield designs that differ substantially from those obtained by optimizing each scale independently.

Niu and Wadbro (2021) later applied this method to the two-scale optimization of structures for vibration suppression. Building on boundary identification (29), the authors reformulate the problem. The new objective is to minimize the dynamic compliance, which quantifies the structural response under time-harmonic excitation. Along with a global and a local volume constraint, the authors also add a static compliance constraint. This constraint helps to avoid statically weak configurations and prevents resonance issues when the excitation frequency exceeds the structure's fundamental resonance frequency. Numerical results are presented for a variety of scenarios, demonstrating the method's robustness with respect to different damping properties, static compliance limits, excitation frequencies, and coating thickness. However, the method shows limitations when applied to high-frequency excitation scenarios.

Around the same time, Yi et al. (2021) proposed an alternative approach for coated structures that eliminates the need to compute the gradient norm of the design field. This approach is based on the two-step filtering proposed by Clausen et al. (2015), but replaces the gradient-norm-based boundary identification with a simple multiplication of filtered designs. Namely, the substrate and the coating are, respectively, identified as

$$\begin{aligned} \mathcal{S}(\alpha) &= \mathcal{P}_1(\mathcal{F}_{r_1}(\alpha)), \quad \text{and} \\ \mathcal{B}(\alpha) &= (1 - \mathcal{S}(\alpha))\mathcal{P}_2(\mathcal{F}_{r_2}(\mathcal{S}(\alpha))), \end{aligned} \quad (30)$$

where  $\mathcal{F}_r$  denotes a PDE filter with radius  $r = r_1, r_2$ ,  $\mathcal{P}_1$  is a tanh-based approximation of a shifted Heaviside function, and  $\mathcal{P}_2$  is a S-shape-inspired scaling function. The authors show how this method differs from the gradient norm approach, particularly by facilitating the change of material state from substrate to coating. Unlike the gradient norm, which vanishes within uniform density regions, their approach varies smoothly with changes in the density field. As a result, it is easier to create coated holes inside the substrate and merge isolated coatings in the design. This is illustrated through visualizations of how the material state evolves inside the design field. Additionally, numerical experiments in both 2D and 3D showcase the method's effectiveness when starting from different initial material distributions. Interestingly, Yi et al. (2021) observe that uniform and non-uniform initial designs produce distinct yet comparable results, likely due to the increased number of local minima introduced by incorporating the coating layer.

Hu et al. (2024) extended previous methods to optimize coated structures with multi-material infill. Both the infill and coating regions are identified as products of filtered designs. However, the infill consists of multiple materials, determined using a piece-wise Heaviside-style mapping (Zuo and Saitou 2017). All the material fields are then interpolated in a SIMP-inspired way.

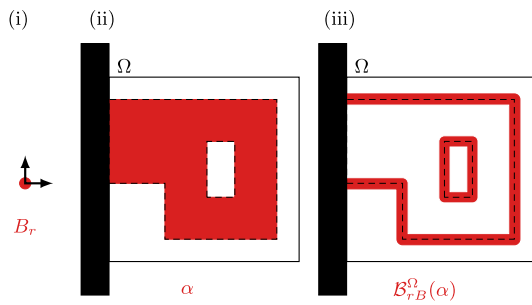


**Fig. 16** The coating layer (iii) computed using boundary strip indicator (31) for a test-case design  $\alpha$  (ii) is displayed. Here,  $\alpha$  is clamped to material (in black) on the left of the design domain  $\Omega$ . The diameter of the structuring element  $B_r$  indicates the thickness of the coating

Motivated by the advancements in additive manufacturing for fiber-reinforced polymer composites, Yang et al. (2024) introduce a method for the topology optimization of a four-phase composite. The four material phases—void, coating, matrix, and fiber layer—are represented using two design variables, following the approach of Wu et al. (2017). The first density field corresponds to the matrix layer, forming part of the substrate, from which the coating is subsequently computed as described by Luo et al. (2019). The second density field indicates the fiber material, reinforcing the matrix material. There are two innovative aspects presented in this work. The first is a dual-variable-scale filtering approach, which enables coating layers with spatially varying thickness, overcoming the limitations of uniform thickness coatings. This was done by drawing inspiration from porous structure optimization techniques presented by Yang et al. (2023). Second, a bilinear interpolation-based smoothing technique is applied to the final design. This effectively smooths jagged borders, improving computational efficiency while preserving high-resolution results, an especially important balance in large-scale optimizations.

Building on the morphology-mimicking nonlinear filters, Setta et al. (2024) proposed a boundary identification method using the  $fW$ -mean erode and dilate filters (see equation (2)). In this approach, the substrate is identified with the eroded design, and the coating layer is identified via a so-called boundary strip indicator given by

$$B_{r,B}^{\Omega}(\alpha) = \mathcal{D}_{rB}^{\Omega}(\alpha) - \mathcal{E}_{rB}^{\Omega}(\alpha). \tag{31}$$

A consequence of this definition is that the identified strip has uniform thickness equal to the chosen diameter of the filters. Unlike indicator (29), this boundary strip indicator is guaranteed to be non-negative, a property proved by the authors. The non-negativity ensures that the identified strip takes values in  $[0, 1]$ .

Figure 16 illustrates the effect of the boundary strip indicator (iii) on a test design  $\alpha$  (ii) in a design domain  $\Omega$

probed with a structuring element  $B_r$  (i). Here, the material is clamped to a fixed wall (in black) on the left of the design domain. The radius  $r$  of the used filters directly controls the thickness of the coating; the coating thickness corresponds to the diameter of the structuring element,  $2r$ . Here, the material interpolation is also inspired by the SIMP method. Moreover, to ensure minimum size control of the substrate, the authors employ an open–close approach (Hägg and Wadbro 2018). Numerical simulations of a heat compliance problem show that the method can identify a uniform coating layer while maintaining a minimum substrate thickness.

### 6.3 Image-inspired boundary detection

Inspired by the pioneer two-step approach (Clausen et al. 2015), Postigo et al. (2024) proposed a boundary identification method using a low-level image processing technique to replace the need for computing design gradients. The idea behind their method is to employ the Smallest Univalued Segment Assimilating Nucleus (SUSAN) algorithm (Smith and Brady 1997). This method differs from those discussed earlier in this section by relying on edge detection rather than element-based indicators. Specifically, the SUSAN algorithm is a nonlinear edge detection method that uses the similarity of values in neighboring elements. The first step is to select a mask domain  $\Omega_S$ , which acts as a structuring element to scan the design domain element by element. Subsequently, the base material is identified as in expression (19). The presence of a boundary in the element  $i$  is then computed as

$$\chi_i = \sum_{j \in \Omega_S} 1 - e^{-\left(\frac{S(\alpha)_i - S(\alpha)_j}{t}\right)^6}, \tag{32}$$

where the threshold  $t$  controls the minimum contrast for edge detection, and the choice of the power 6 is discussed by Smith and Brady (1997). The coating layer is identified by filtering the boundary field  $\chi$ . The substrate is then interpolated accordingly to avoid overlap with the coating. Furthermore, this approach can be extended to shell-infill structures by introducing an additional design variable for the infill field. In this extended approach, the non-uniform infill is filtered and interpolated within the coating region, replacing the uniform infill assumption. Designs generated with this method show the SUSAN algorithm’s ability to precisely detect the structural contours.

Recently, Wang et al. (2025) proposed a further development of the two-step filtering method for shell-infill structures. To enhance static load capabilities and reduce low-frequency vibrations, the authors define the objective as a weighted sum of compliance and fundamental frequency. A key innovation is the use of a Gaussian function in bound-

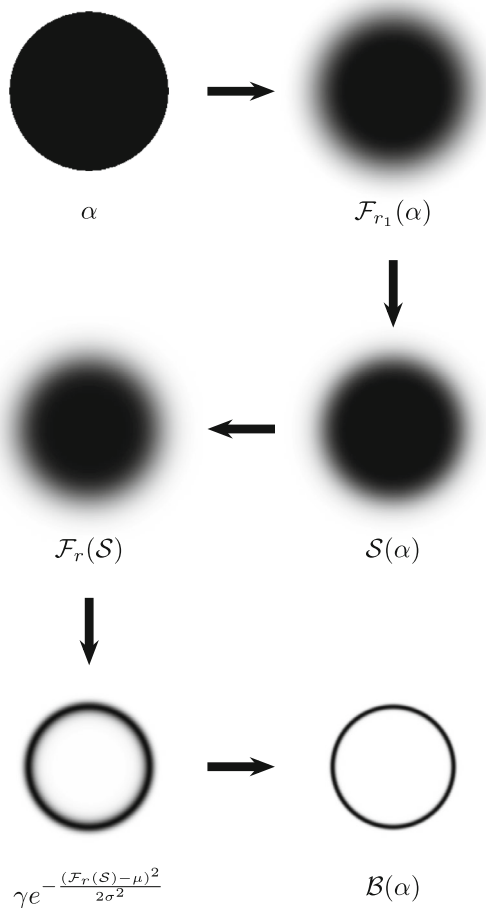


**Fig. 17** Two-step filtering workflow as described by Wang et al. (2025). Here, the test-case design  $\alpha$  is processed and scaled to identify the coating layer  $\mathcal{B}(\alpha)$

ary identification; this function maps intermediate density values after two-step filtering to enable precise shell extraction. The authors derive an explicit relationship between the shell thickness, the Gaussian parameters, and the filter radius, offering theoretical insight into thickness control. While the substrate is identified as in (19), the shell is identified by a processed Gaussian function as

$$\mathcal{B}(\alpha) = \mathcal{P}_{\beta, \eta} \left( \gamma e^{-\frac{(F_r(S) - \mu)^2}{2\sigma^2}} \right), \tag{33}$$

where  $r$  is the filter radius,  $\beta$  and  $\eta$  are scaling parameters, and  $\gamma, \mu,$  and  $\sigma$  define the Gaussian function.

Figure 17 shows the filtering strategy to identify the boundary  $\mathcal{B}(\alpha)$  for a test-case design  $\alpha$ . This approach follows the two-step strategy introduced by Clausen et al. (2015)—resulting in the workflow shown in Fig. 15—but replaces the substrate’s gradient with a Gaussian function. Their study further reveals how the shell thickness depends on these Gaussian parameters, allowing precise design con-

tol. Another important contribution is the introduction of a Solid Isotropic Material with Variable Penalization (SIMVP) interpolation scheme, using a differentiable function that varies the penalization with the local density. This formulation addresses the inconsistency between stiffness and mass penalization in low-density regions, effectively mitigating pseudo modes that commonly arise in frequency-based topology optimization.

### 7 Problems with layers

Assume that a surface  $\Gamma$  cuts through a domain  $\Omega$ , dividing it into two nonintersecting subdomains  $\Omega_1$  and  $\Omega_2$ . These subdomains are either provided with the same governing equations but hosting different physical properties, such as different materials, or there are entirely different equations in the subdomains, coupled through transmission conditions at  $\Gamma$ .

A common feature in such cases is the occurrence of domain layers in the vicinity of the interface  $\Gamma$  (Fig. 18). The most well-known example is perhaps the laminar or turbulent boundary layers occurring in fluid mechanics. These boundary layers also occur for wave propagation in fluids. Another example is the skin effect in metals subject to a high-frequency current. In these cases, the characteristic length scale within the layer is much smaller than in the rest of the domain. Therefore, accurate numerical results require special treatments, such as mesh refinements around the interface  $\Gamma$ . When carrying out design optimization for such problems, it is most straightforward to use techniques in which the interface remains well-defined throughout the optimization, for instance, using level-set methods with body-fitted meshes (Tissot et al. 2020; Noguchi and Yamada 2022), or formulating the problem on the interface itself using integral equations (Andersen et al. 2019). However, reliance on methods using conforming meshes can restrict geometric generality and limit the design space. Moreover, re-meshing or mesh adaptation is required to track the evolving interface, which substantially increases the computational cost and often makes these approaches impractical for large-scale or broadband applications. In contrast, material distribution methods offer much greater geometric flexibility, as the interface can evolve freely on a fixed mesh. This allows for the use of a Cartesian mesh for the design variable, avoiding mesh-induced bias; however, accurately resolving thin boundary layers still requires local mesh refinement, adding complexity and potentially leading to premature convergence to suboptimal designs.

If the effects of these layers on the surrounding field could be accurately modeled—for instance, through a boundary condition—it would be possible to avoid mesh refinement and instead use a coarse Cartesian mesh with interface con-

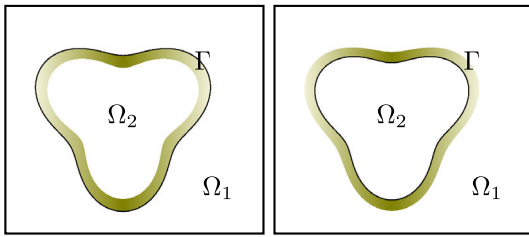


**Fig. 18** A surface  $\Gamma$  divides a domain into two subdomains, where a layer phenomenon occurs in the inner domain  $\Omega_2$  (left), or in the outer domain  $\Omega_1$  (right)

ditions that capture the boundary layer behavior. An example of such conditions is the use of *wall functions* in Computational Fluid Dynamics (CFD), which eliminate the need to explicitly resolve near-wall phenomena in the boundary layers when employing Reynolds-Averaged Navier–Stokes (RANS) models. However, wall functions have rarely been applied at evolving interfaces within material distribution topology optimization. Instead, existing studies apply wall functions only at fixed domain boundaries, while solid regions are effectively represented as low-porosity materials by introducing penalization terms in the momentum equations to suppress velocity (Dilgen et al. 2018; Tian et al. 2024). Analogous penalization is used for turbulence closure equations—such as those governing the turbulent kinetic energy and specific dissipation rate in the  $k$ – $\omega$  model—to enforce prescribed values within the solid region (Dilgen et al. 2018). As a result, the boundary layers at the solid–fluid interface must be directly resolved through the mesh. Consequently, either a globally refined mesh is used, which significantly increases the computational cost, or the boundary layer at the evolving solid–fluid interface remains under-resolved. To the best of the authors’ knowledge, the recent preprint by Bayat et al. (2026b) is the first to incorporate wall functions directly at evolving interfaces in a material distribution topology optimization framework, employing the standard  $k$ – $\varepsilon$  RANS model alongside an implicit wall-penalty treatment.

Another related but distinct line of work uses the one-equation Spalart–Allmaras turbulence model (Spalart and Allmaras 1992), in which the wall-distance field enters explicitly. A few studies have used this model in the context of topology optimization, where the wall-distance field is computed by solving a modified Eikonal or Poisson-like equation that accounts for the evolving solid boundaries throughout the optimization (Yoon 2016; Dilgen et al. 2018; Sá et al. 2021; Garcia-Rodriguez et al. 2022). While this strategy incorporates the influence of emerging walls through the wall-distance field, it does not impose wall-function-type interface conditions at evolving solid–fluid boundaries. Moreover, despite its numerical efficiency, the baseline Spalart–Allmaras model has been shown to exhibit lim-

ited accuracy in several flow regimes, and thus may lack robustness for topology optimization problems involving transitional or separated turbulent flows (Yusuf et al. 2020; Bayat et al. 2026b).

Similarly, in conjugate heat transfer problems, an interpolation for the thermal conductivity is used in the heat transfer equation together with a penalty term that can be interpreted as a velocity-dependent heat sink (Haertel and Nellis 2017; Wang et al. 2025; Zhang et al. 2023). In this way, the convective term in the heat transport equation is effectively damped within the solid region due to the low velocity magnitude, without any explicit treatment at the interface. Thus, in material distribution topology optimization for CFD problems, boundary layers at the evolving interface are typically treated either through under-resolved but computationally efficient models, or through adaptive meshing that explicitly resolves them at a substantial increase in computational cost. Only a few studies in CFD have employed interface identification methods to impose specific boundary conditions. For instance, a recent article by Bayat et al. (2026a) uses a double-filtering approach to apply slip-free conditions within a material distribution topology optimization framework.

In contrast, there are applications in electromagnetic and acoustic wave propagation for which accurate approximate models, in many cases, remove the need to mesh-resolve the layers (Aage et al. 2010; Mousavi et al. 2023; Mirpourian and Aage 2025a). We will consider two such examples, illustrated in the left and right pictures of Fig. 18:

1. Let  $\Omega_1$  be free space characterized by vacuum permittivity  $\epsilon_0$  and permeability  $\mu_0$  and  $\Omega_2$  a conducting material with permittivity  $\epsilon = \epsilon_r \epsilon_0$ , permeability  $\mu = \mu_r \mu_0$ , and conductivity  $\sigma$ . An electromagnetic wave with angular frequency  $\omega$  will propagate unimpeded through  $\Omega_1$  but will be damped by ohmic losses inside  $\Omega_2$ . The propagation depth into  $\Omega_2$  is characterized by the *skin depth* parameter (Hayt and Buck 2019, § 11.4.2)

$$\delta = \sqrt{\frac{2}{\mu\sigma\omega}}, \quad (34)$$

which in conductors will be several orders of magnitude smaller than the free-space wavelength of radio- and microwave radiation.

2. Let  $\Omega_1$  be still air in which acoustic waves propagate. The complementary domain  $\Omega_2$  is a solid, either perfectly rigid or made out of elastic material. Boundary layers will typically form in  $\Omega_1$  in the vicinity of  $\Gamma$ . For instance, when  $\Omega_2$  is perfectly rigid, the velocity field will vanish at  $\Gamma$ , causing tangential momentum loss close to the wall due to air viscosity. Also, since solid materials have a higher

thermal conductivity than air, a good approximation is that the acoustic temperature fluctuations in  $\Omega_1$  vanish at  $\Gamma$ , causing a small heat flow into the wall. The thickness of these *viscothermal* (also called *thermoviscous*) layers in  $\Omega_1$  close to  $\Gamma$  is characterized by the viscous and thermal boundary layer thicknesses (Pierce 1981, Ch. 10-4)

$$\delta_V = \sqrt{\frac{2\nu}{\omega}}, \quad \delta_T = \sqrt{\frac{2\kappa}{\omega\rho_0c_p}}, \tag{35}$$

where  $\nu$  is the kinematic viscosity,  $\kappa$  the thermal conductivity,  $\rho_0$  the static density,  $c_p$  the specific heat at constant pressure, and  $\omega$  the frequency of the wave in  $\Omega_1$ . Under atmospheric conditions and for frequencies in the audio range, the viscothermal boundary layer thicknesses are smaller than the wavelength by a factor of approximately  $10^{-6}$ – $10^{-3}$  (low to high frequency).

Accurate computations from first principles in both these cases require mesh refinements close to  $\Gamma$  in  $\Omega_2$  in case 1 and  $\Omega_1$  in case 2. A practical remedy for this complication is the use of an *impedance boundary condition* at  $\Gamma$ , which accurately approximates the exact conditions in many important cases, without the need to resolve the layers.

By specifying the appropriate variational forms used to define the finite-element matrices, we will detail below how such boundary conditions can be used in practical computations. Perhaps surprisingly, the boundary conditions enter into the equations in a similar manner in the two cases above. We will provide expressions that explicitly highlight the similarity, since the analogy between the cases is far from obvious when consulting original sources, such as Aage et al. (2010) and Mousavi et al. (2023), where such boundary conditions are used in the context of material distribution topology optimization. Highlighting the analogy is an original contribution of this review.

For case 1 above, the appropriate impedance condition at  $\Gamma$ , as derived, for instance, by Senior (1960), is

$$\mathbf{E}_t + Z\mathbf{n} \times \mathbf{H} = 0, \tag{36}$$

where  $\mathbf{E}$  and  $\mathbf{H}$  are the electric and magnetic fields, respectively,  $\mathbf{n}$  the unit normal vector at  $\Gamma$  pointing into  $\Omega_2$ ,  $\mathbf{E}_t = \mathbf{E} - (\mathbf{n} \cdot \mathbf{E})\mathbf{n}$  the tangential components of  $\mathbf{E}$  along  $\Gamma$ , and  $Z = Z_0Z_r$ , where

$$Z_0 = \sqrt{\frac{\mu_0}{\epsilon_0}}, \quad Z_r = \sqrt{\frac{\mu_r}{\epsilon_r + i\frac{\sigma}{\epsilon_0\omega}}}, \tag{37}$$

is the equivalent impedance at  $\Gamma$  due to the skin effect in  $\Omega_2$ .

Assume now that we aim for a finite-element discretization of the frequency-domain Maxwell equations formulated

in the electric field  $\mathbf{E}$ . For this, we first need to obtain a variational formulation of the boundary value problem. In this case, subject to impedance boundary condition (36), the electric field in  $\Omega_1$  satisfies the following variational problem, for each test function  $\mathbf{F}$ ,

$$\int_{\Omega_1} \nabla \times \mathbf{E} \cdot \nabla \times \mathbf{F} \, dV - k_0^2 \int_{\Omega_1} \mathbf{E} \cdot \mathbf{F} \, dV + ik_0 \int_{\Gamma} Y_r \mathbf{E}_t \cdot \mathbf{F}_t \, dS + \dots = 0, \tag{38}$$

where  $Y_r = 1/Z_r$  is the relative admittance at  $\Gamma$ . The ellipsis in equation (38) signifies additional terms such as input or output ports. The boundary integral in equation (38) accounts for the ohmic losses in  $\Omega_2$  caused by the skin effect.

Analogous expressions also hold in acoustics for case 2 above. An appropriate boundary condition on  $\Gamma$ , capturing the viscous and thermal boundary layers in  $\Omega_1$  is

$$Yp - \mathbf{n} \cdot \mathbf{u} = 0. \tag{39}$$

Here,  $p$  and  $\mathbf{u}$  are the acoustic pressure and velocity, respectively. Moreover,  $Y = Y_r/Z_0$ , where  $Z_0 = \rho_0c_0$  is the acoustic plane wave impedance, an acoustic analogue to the impedance of free space (37) in electromagnetics;  $c_0$  is the acoustic phase velocity in air. In acoustics, the relative viscothermal admittance is a more complicated object than its electromagnetic analogue; it can be written

$$Y_r p = -\frac{\delta_V}{k_0} \sqrt{\frac{i}{2}} \Delta_{\Gamma} p + \delta_T k_0 \sqrt{\frac{i}{2}} (\gamma - 1) p, \tag{40}$$

where  $k_0 = \omega/c_0$  is the wavenumber,  $i$  is the imaginary unit,  $\sqrt{i} = (i + 1)/\sqrt{2}$ , and  $\Delta_{\Gamma} = \Delta - \partial^2/\partial n^2$  is the tangential Laplacian. That is,  $Y$  is a surface diffusion–reaction operator and not just a complex number as in the skin-depth model.

The origins of model (39)–(40) trace back to Cremer (1948), who devised a version of the model for plane waves impinging at an angle on the wall. A boundary condition equivalent to (39) is given in the classic book by Pierce (1981, eq. (10–4.12)) and was first typically used to estimate total energy losses, not as a tool for computational acoustics. The model as a boundary condition to the Helmholtz equation for computational purposes has later been independently reinvented many times, with a particular flood of publications in 2018 (Nijhof 2010; Cheng et al. 2013; Inoue and Sakuma 2018; Berggren et al. 2018; Bach and Bruus 2018; Jith and Sarkar 2018; Schmidt and Thöns-Zueva 2022); some of these only consider the viscous layer.

The Helmholtz equation subject to boundary condition (39) gives rise to the following variational problem for

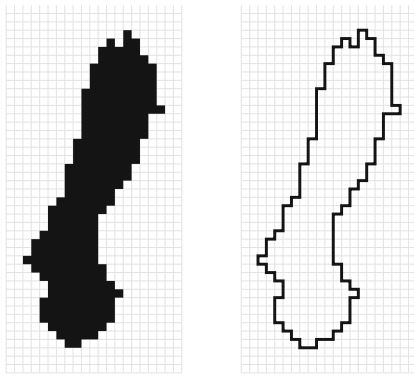


**Fig. 19** Left: An arbitrary design defined in a structured mesh of square elements by an element-wise constant material indicator function  $\alpha$ , where one material is represented by elements filled with black and the other with empty elements. Right: Identifying the material interface using a face-wise constant boundary indicator function  $\eta = \llbracket \alpha \rrbracket^2$ , that is, the square of the jump of  $\alpha$  between elements sharing a common face. Indicator function  $\eta$  is defined on all edges in the mesh;  $\eta = 1$  is illustrated by thick black lines and  $\eta = 0$  by thin gray lines

the acoustic pressure

$$\int_{\Omega_1} \nabla p \cdot \nabla q \, dV - k_0^2 \int_{\Omega_1} pq \, dV + ik_0 \langle Y_r p, q \rangle_{\Gamma} + \dots = 0, \tag{41}$$

for each test function  $q$ . The loss term in equation (41) is written in a way that pinpoints the formal analogue to equation (38). In practice, the term will be evaluated after integration by parts, that is,

$$ik_0 \langle Y_r p, q \rangle_{\Gamma} = \delta_V \frac{i-1}{2} \int_{\Gamma} \nabla_{\Gamma} p \cdot \nabla_{\Gamma} q \, dS + \delta_T k_0^2 \frac{(i-1)(\gamma-1)}{2} \int_{\Gamma} pq \, dS, \tag{42}$$

where  $\nabla_{\Gamma} = \nabla - \mathbf{n} \partial/\partial n$  is the tangential gradient along  $\Gamma$ .

In both cases introduced above, we have thus reached variational problems that model the effects of layers. In applications where loss effects are important to account for, these formulations are convenient to use for topology optimization, since the effects of the layers are provided through the surface admittance  $Y_r$  without the need for mesh refinements around  $\Gamma$ .

To integrate model (41) into a material distribution topology optimization framework, Mousavi et al. (2023) devised a face-based indicator function derived from jumps in element-wise constant material indicator functions as illustrated in Fig. 19.

Using this indicator function and extending variational forms (41)–(42), we reach a formulation allowing for material distribution topology optimization for viscothermal acoustics. This is done by optimization over material indica-

tor  $\alpha \in [\epsilon, 1]$  in

$$\int_{\Omega} \alpha \nabla p \cdot \nabla q \, dV - k_0^2 \int_{\Omega} \alpha pq \, dV + \delta_V \frac{i-1}{2} \int_{\Sigma} \llbracket \alpha \rrbracket^2 \nabla_{\Gamma} p \cdot \nabla_{\Gamma} q \, dS + \delta_T k_0^2 \frac{(i-1)(\gamma-1)}{2} \int_{\Sigma} \llbracket \alpha \rrbracket^2 pq \, dS = 0, \tag{43}$$

where  $\Sigma$  is the set of all mesh faces. Using this approach, Mousavi et al. (2023) designed Helmholtz-resonator-like damping devices and Mousavi et al. (2024) waveguide sonic black holes.

A related approach was earlier proposed by Aage et al. (2010) for lossy electromagnetics, case 1 above. Consider again an element-wise-constant material indicator function  $\alpha$  where now  $\alpha = 0$  represents a lossless dielectric and  $\alpha = 1$  a non-ideal, lossy conductor. Variational problem (38) can be adjusted to this case, and when restricted to a single element  $K$  in a mesh, it will read

$$\int_K \mu_r^{-1}(\alpha) \nabla \times \mathbf{E} \cdot \nabla \times \mathbf{F} \, dV - k_0^2 \int_K \epsilon_c(\alpha) \mathbf{E} \cdot \mathbf{F} \, dV + ik_0 \int_{\partial K} f(\alpha) Y_r \mathbf{E}_t \cdot \mathbf{F}_t \, dS = 0, \tag{44}$$

where

$$\epsilon_c = \epsilon_r - \frac{i\sigma}{\omega\epsilon_0}. \tag{45}$$

As signified by the notation, the values of parameters  $\mu_r$ ,  $\epsilon_c$ , and  $f$  depend on the material content in  $K$ . Note, in particular, that  $\sigma = 0$ ,  $\mu_r = \epsilon_r = 1$  when  $\alpha = 0$ , that is, inside the lossless dielectric. Moreover, the function  $f$  will be defined so that  $f(0) = 0$ , and  $f(1) = 1$ , which means that the boundary loss term in equation (44) vanishes for each element contained in the dielectric but is present for each element in the conductor. Summing up variational problem (44) over all elements in the mesh, it follows that the correct variational problem will be specified in the dielectric. In particular, the boundary loss term will be present at the dielectric–conductor boundary but not for faces strictly inside the dielectric.

To solve the topology optimization problem, equation (44) needs to be well defined also for intermediate values of  $\alpha$ . Aage et al. (2010) provide sophisticated interpolation schemes for all the parameters. The final variational problem will be analogous to the acoustic problem (43) but without the squaring of the material indicator. This approach has been used in the optimization of various devices such as resonators (Aage et al. 2010) and microwave waveguide filters (Aage and Johansen 2017).

Finally, *non-physical* layer effects may occur due to inappropriate material interpolation schemes. A case in point is the interpolation between a dielectric and a metal in optical regimes supporting plasmonic resonances. Here, the interpolation is carried out in the complex plane between a low-loss material with a positive dielectric constant and a lossy material with a *negative* dielectric constant. Christiansen et al. (2019) demonstrate that simple interpolation schemes can produce artificial field enhancements for intermediate values of the interpolation parameter, and the authors propose a nonlinear interpolation scheme with superior properties.

## 8 Concluding discussion

Boundary-effect-dominated problems in topology optimization present a multifaceted landscape of challenges and opportunities. This review has traced the historical development and contemporary strategies for addressing such problems within the material distribution framework, highlighting the field's evolution. We have surveyed a broad spectrum of approaches that tackle boundary effects in topology optimization. Each section has emphasized the interplay between physical modeling, optimization formulation, and numerical treatment, underscoring the need for careful boundary treatment when boundaries significantly influence the governing physics. Over the last decades, boundary identification—whether through filtering, image processing, or gradient-based techniques—has become central to enable topology optimization in settings where traditional assumptions break down. The incorporation of impedance boundary conditions and face-based indicators further expands the applicability of material distribution methods to problems involving thin layers and complex boundary phenomena.

Across the reviewed methods, several trends emerge. Filtering-based approaches offer flexibility and scalability, but achieving sharp interfaces often requires a continuation strategy for the filtering parameters. Image-processing-inspired methods offer intuitive and robust boundary detection, but often lack the mathematical rigor and generalizability of PDE-based approaches. Impedance modeling and face-based indicators provide a promising approach to incorporating boundary layers for certain applications, but rely on accurate physical modeling and interpolation schemes.

Despite substantial progress, several challenges remain. Accurate and efficient identification of evolving boundaries continues to be a bottleneck. Furthermore, the integration of high-fidelity physical models, such as those involving impedance boundary conditions, into scalable optimization frameworks remains a challenge, especially when computational cost is a concern. Another major challenge is the limited availability of standardized benchmark problems tailored to boundary-sensitive applications. Unlike classical

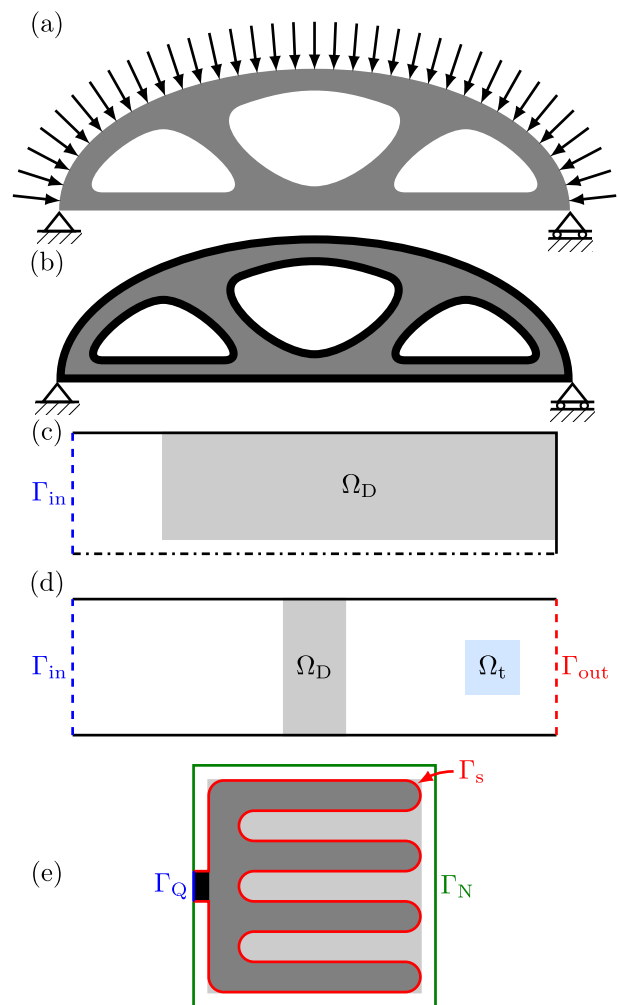


**Fig. 20** Illustrations of five different possible benchmark problems structural optimization problems in linear elasticity, such as compliance minimization, where canonical test cases are well established, the diversity of physical settings and modeling assumptions for boundary-effect-dominated problems complicates method comparison on a common basis. The lack of benchmarks also hampers reproducibility, slows methodological progress, and limits the ability to rigorously assess new approaches. Therefore, establishing representative benchmark problems is essential for improving reproducibility, enabling rigorous and fair method comparison, and accelerating further development in this diverse field. The following problems illustrate typical boundary-effect scenarios spanning different physical domains. Although not standardized yet, they provide a practical foundation for testing and comparing methods and could serve as a basis for future standardization efforts.

- **MBB-type beam with surface pressure loading:** The MBB-type beam is a well-known benchmark problem for various types of standard compliance topology optimization. To establish a structural optimization benchmark tai-

lored for boundary-effect investigations, the prescribed design-independent traction force can be replaced by a design-dependent pressure loading. Thus, the boundary-effect study for this type of problem is straightforward to extend from standard compliance topology optimization. Figure 20a illustrates a beam that connects the two supports along the left and right sides of the bottom of the domain and is subject to a distributed pressure load on its top surface, introducing a design-dependent traction boundary.

- **Coated structures benchmarks:** For coated structures, we lift two possible benchmark problems with similar features that explore different aspects of boundary-dominated behavior. The first problem is already a standard benchmark and a natural extension of the classic minimal compliance benchmark, with the addition that the design must have a coating layer of a prescribed thickness, see Fig. 20b. This setup retains the simplicity of standard compliance test problems, while tracking the evolving boundary and evaluating its effects on the design throughout the optimization. This provides a controlled environment for evaluating methods that must accurately identify and update an evolving layer. An alternative benchmark introduces additional complexity by combining the coating requirement with design-dependent pressure loading, as described in the first benchmark. In this scenario, coupling the evolution of the coating interface with the pressure boundary stresses the need for accurate boundary identification and modeling. Together, these benchmark problems illustrate the main challenges of coated-structure problems: capturing boundary layers, preserving the required coating thickness, and consistently identifying interfaces on designs that can change topology.
- **Acoustic problem with viscothermal losses:** Figure 20c illustrates a waveguide with an incoming right-going wave at the left boundary. The acoustic wave propagation is subject to viscothermal losses, which are modeled using impedance boundary conditions. The design task is to determine the optimal material layout in  $\Omega_D$  to achieve a desired acoustic effect. Two benchmark variations are possible depending on the chosen objective:
  1. Maximizing acoustic energy dissipation within a cavity acting as an absorber (Noguchi and Yamada 2022).
  2. Focusing the acoustic energy in a small region on the right side, minimizing the losses and creating a so-called acoustic black-hole effect (Mousavi et al. 2024).
- **Vibroacoustic problem:** Figure 20d shows the acoustic partitioner problem, in which an acoustic waveguide is divided by a flexible partition. An incoming plane wave is prescribed at the inlet  $\Gamma_{in}$ , propagating from left to right.

The aim is to distribute a given amount of flexible material within the design domain  $\Omega_D$  so as to minimize the integral of acoustic amplitude in the target region  $\Omega_t$  on the right-hand side (Yoon et al. 2007; Dilgen et al. 2021; Mirpourian and Aage 2025b).

- **Newtonian cooling heat sink:** Heat convection often varies across the structure's interface, and it is usually difficult to incorporate it into a standard topology optimization scheme. Fortunately, this phenomenon can be taken into account by using the classic thermal compliance topology optimization with an additional boundary condition of Newtonian cooling (11) on the design's exposed surfaces. Figure 20e illustrates the design domain, where a given incoming heat flux enters at  $\Gamma_Q$  marked in blue and the Newtonian cooling takes place on the interface  $\Gamma_s$  marked in red. The convection boundary strongly affects the steady-state thermal behavior, and the objective is to maximize cooling by minimizing the temperature at  $\Gamma_D$ . Therefore, this problem can be considered as a benchmark problem due to its implementation simplicity.

Beyond the topics reviewed in this article, several emerging challenges in the context of boundary-effect-dominated topology optimization are gaining attention. These include elastic and thermoelastic contact problems (Bluhm et al. 2021; Dalklint et al. 2023; Frederiksen et al. 2024, 2025; Dalklint et al. 2025) and multiphysics scenarios involving fluid–structure interaction under design-dependent conditions. In material distribution topology optimization, fluid–structure interaction problems are typically handled without explicit interface tracking, by reformulating interface tractions and pressure loads as equivalent volume contributions through weak-form manipulations and indicator functions defined on a fixed mesh. Early material distribution formulations for fluid–structure interaction date back more than 15 years (Yoon 2010; Kreissl et al. 2010; Yoon 2014). Subsequent work has refined these ideas, revisited material interpolation, coupling consistency, and numerical robustness (Lundgaard et al. 2018), and extended them to transient and more general settings (Picelli et al. 2020; Yoon 2023; Abdelhamid and Czekanski 2024; Hederberg and Thore 2025). Another direction for improving boundary treatment is to increase the resolution near interfaces using partial element formulations (Zhou et al. 2025) or adaptive mesh refinement techniques (Nana et al. 2016; Salazar de Troya and Tortorelli 2018; Mezzadri and Qian 2022; Herrero-Pérez et al. 2024).

Boundary effects are no longer peripheral concerns in topology optimization—they are central to the design of high-performance structures in fluid-dynamics, electromagnetics, acoustics, and thermal systems. As the field continues to grow, the integration of boundary-aware methods, scalable optimization frameworks, and high-fidelity physical modeling will be crucial. To conclude, boundary effects represent a

frontier in topology optimization—where physics, geometry, and computation converge—and future advances will likely redefine the limits of what can be designed.

**Author Contributions** All authors contributed equally to this article.

**Funding** Open access funding provided by Karlstad University. This work was financially supported by the Swedish Research Council (grant 2022-03783) and by the Swedish strategic research program eSSENCE.

## Declarations

**Conflict of interest** The authors declare that they have no known competing financial interests or personal relationships that could have appeared to influence the work reported in this paper.

**Replication of results** We have cited original sources that include implementation details, data, and methodologies to support the reproducibility of the referenced results.

**Open Access** This article is licensed under a Creative Commons Attribution 4.0 International License, which permits use, sharing, adaptation, distribution and reproduction in any medium or format, as long as you give appropriate credit to the original author(s) and the source, provide a link to the Creative Commons licence, and indicate if changes were made. The images or other third party material in this article are included in the article's Creative Commons licence, unless indicated otherwise in a credit line to the material. If material is not included in the article's Creative Commons licence and your intended use is not permitted by statutory regulation or exceeds the permitted use, you will need to obtain permission directly from the copyright holder. To view a copy of this licence, visit <http://creativecommons.org/licenses/by/4.0/>.

## References

- Aage N, Johansen VE (2017) Topology optimization of microwave waveguide filters. *Internat J Numer Methods Engrg* 112:283–300. <https://doi.org/10.1002/nme.5551>
- Aage N, Mortensen NA, Sigmund O (2010) Topology optimization of metallic devices for microwave applications. *Internat J Numer Methods Engrg* 83(2):228–248. <https://doi.org/10.1002/nme.2837>
- Aage N, Andreassen E, Lazarov BS, Sigmund O (2017) Gigavoxel computational morphogenesis for structural design. *Nature* 550(7674):84–86. <https://doi.org/10.1038/nature23911>
- Abdelhamid M, Czekanski A (2024) Topology optimization of fluid-structure interaction problems with total stress equilibrium. *Internat J Numer Methods Engrg* 125(2):e7368. <https://doi.org/10.1002/nme.7368>
- Alexandersen J (2011) Topology optimization for convection problems. Bachelor's thesis, Technical University of Denmark, available at: <https://portal.findresearcher.sdu.dk/en/publications/topology-optimization-for-convection-problems> (accessed 2026–02–02)
- Alexandersen J, Andreasen CS (2020) A review of topology optimisation for fluid-based problems. *Fluids* 5:29. <https://doi.org/10.3390/fluids5010029>
- Andersen PR, Cutanda Henríquez V, Aage N (2019) Shape optimization of micro-acoustic devices including viscous and thermal losses. *J Sound Vibration* 447:120–136. <https://doi.org/10.1016/j.jsv.2019.01.047>
- Baandrup M, Sigmund O, Polk H, Aage N (2020) Closing the gap towards super-long suspension bridges using computational morphogenesis. *Nat Commun* 11:2735. <https://doi.org/10.1038/s41467-020-16599-6>
- Bach JS, Bruus H (2018) Theory of pressure acoustics with viscous boundary layers and streaming in curved elastic cavities. *J Acoust Soc Amer* 144(2):766–784. <https://doi.org/10.1121/1.5049579>
- Banh TT, Lee D (2024) Comprehensive polygonal topology optimization for triplet thermo-mechanical-pressure multi-material systems. *Engrg Comput* 40(5):3295–3317. <https://doi.org/10.1007/s00366-024-01982-4>
- Bar-Cohen A, Rohsenow WM (1984) Thermally optimum spacing of vertical, natural convection cooled, parallel plates. *J Heat Transf* 106(1):116–123. <https://doi.org/10.1115/1.3246622>
- Bayat A, Li H, Alexandersen J (2026) Density-based topology optimization for Navier-Stokes flow with free-slip boundary conditions. *Struct Multidiscip Optim* 69:23. <https://doi.org/10.1007/s00158-025-04212-7>
- Bayat A, Li H, Alexandersen J (2026b) Density-based topology optimization for turbulent fluid flow using the standard k-epsilon rans model with wall-functions imposed through an implicit wall penalty formulation. Available at: <https://arxiv.org/abs/2601.02202> (accessed 2026–02–02)
- Bendsøe MP (1989) Optimal shape design as a material distribution problem. *Struct Opt* 1:193–202. <https://doi.org/10.1007/BF01650949>
- Bendsøe MP, Kikuchi N (1988) Generating optimal topologies in structural design using a homogenization method. *Comput Methods Appl Mech Engrg* 71:197–224. [https://doi.org/10.1016/0045-7825\(88\)90086-2](https://doi.org/10.1016/0045-7825(88)90086-2)
- Bendsøe MP, Sigmund O (1999) Material interpolation schemes in topology optimization. *Arch Appl Mech* 69(9):635–654. <https://doi.org/10.1007/s004190050248>
- Bendsøe MP, Sigmund O (2003) *Topology Optimization. Theory, Methods, and Applications*. Springer
- Berggren M, Bernland A, Noreland D (2018) Acoustic boundary layers as boundary conditions. *J Comput Phys* 371:633–650. <https://doi.org/10.1016/j.jcp.2018.06.005>
- Bernland A, Wadbro E, Berggren M (2018) Acoustic shape optimization using cut finite elements. *Internat J Numer Methods Engrg* 113:432–449. <https://doi.org/10.1002/nme.5621>
- Bluhm GL, Sigmund O, Poulos K (2021) Internal contact modeling for finite strain topology optimization. *Comput Mech* 67(4):1099–1114. <https://doi.org/10.1007/s00466-021-01974-x>
- Borrvall T (2001) Topology optimization of elastic continua using restriction. *Arch Comput Methods Engrg* 8(4):351–385. <https://doi.org/10.1007/BF02743737>
- Borrvall T, Petersson J (2003) Topology optimization of fluids in Stokes flow. *Internat J Numer Methods Fluids* 41:73–187. <https://doi.org/10.1002/fld.426>
- Bourdin B (2001) Filters in topology optimization. *Internat J Numer Methods Engrg* 50:2143–2158. <https://doi.org/10.1002/nme.116>
- Bourdin B, Chambolle A (2003) Design-dependent loads in topology optimization. *ESAIM Control Optim Calc Var* 9:19–48. <https://doi.org/10.1051/cocv:2002070>
- Bruns TE (2007) Topology optimization of convection-dominated, steady-state heat transfer problems. *Int J Heat Mass Tran* 50(15):2859–2873. <https://doi.org/10.1016/j.ijheatmasstransfer.2007.01.039>
- Bruns TE, Tortorelli DA (2001) Topology optimization of non-linear elastic structures and compliant mechanisms. *Comput Methods Appl Mech Engrg* 190:3443–3459. [https://doi.org/10.1016/S0045-7825\(00\)00278-4](https://doi.org/10.1016/S0045-7825(00)00278-4)
- Burman E, Hansbo P (2011) Fictitious domain finite element methods using cut elements: II. A stabilized Nitsche method. *Appl Numer Math* 62:328–341. <https://doi.org/10.1016/j.apnum.2011.01.008>
- Burman E, Claus S, Hansbo P, Larson MG, Massing A (2015) Cut-FEM: discretizing geometry and partial differential equations. *Int*

- J Numer Meth Eng 104(7):472–501. <https://doi.org/10.1002/nme.4823>
- Burman E, Elfverson D, Hansbo P, Larson MG, Larsson K (2018) Shape optimization using the cut finite element method. *Comput Methods Appl Mech Eng* 328:242–261. <https://doi.org/10.1016/j.cma.2017.09.005>
- Cai Y, Xu L, Cheng G (2014) Novel numerical implementation of asymptotic homogenization method for periodic plate structures. *Internat J Solids Structures* 51(1):284–292. <https://doi.org/10.1016/j.ijsolstr.2013.10.003>
- Chen BC, Kikuchi N (2001) Topology optimization with design-dependent loads. *Finite Elem Anal Des* 37(1):57–70. [https://doi.org/10.1016/S0168-874X\(00\)00021-4](https://doi.org/10.1016/S0168-874X(00)00021-4)
- Cheng L, Li Y, Grosh K (2013) Including fluid shear viscosity in a structural acoustic finite element model using a scalar fluid representation. *J Comput Phys* 247:248–261. <https://doi.org/10.1016/j.jcp.2013.03.063>
- Christiansen RE, Vester-Petersen J, Madsen SP, Sigmund O (2019) A non-linear material interpolation for design of metallic nanoparticles using topology optimization. *Comput Methods Appl Mech Engrg* 343:23–39. <https://doi.org/10.1016/j.cma.2018.08.034>
- Chu S, Xiao M, Gao L, Li H, Zhang J, Zhang X (2019) Topology optimization of multi-material structures with graded interfaces. *Comput Methods Appl Mech Engrg* 346:1096–1117. <https://doi.org/10.1016/j.cma.2018.09.040>
- Clausen PM, Sigmund O (2006) The pressure load problem re-visited. In: Bendsøe MP, Olhoff N, Sigmund O (eds) *IUTAM Symposium on Topological Design Optimization of Structures, Machines and Materials*. Springer, Netherlands, Dordrecht, pp 261–267. [https://doi.org/10.1007/1-4020-4752-5\\_26](https://doi.org/10.1007/1-4020-4752-5_26)
- Clausen A, Andreassen E (2017) On filter boundary conditions in topology optimization. *Struct Multidiscip Optim* 56(5):1147–1155. <https://doi.org/10.1007/s00158-017-1709-1>
- Clausen A, Aage N, Sigmund O (2015) Topology optimization of coated structures and material interface problems. *Comput Methods Appl Mech Engrg* 290:524–541. <https://doi.org/10.1016/j.cma.2015.02.011>
- Clausen A, Aage N, Sigmund O (2016) Exploiting additive manufacturing infill in topology optimization for improved buckling load. *Eng (Beijing)* 2(2):250–257. <https://doi.org/10.1016/J.ENG.2016.02.006>
- Clausen A, Andreassen E, Sigmund O (2017) Topology optimization of 3d shell structures with porous infill. *Acta Math Sinica* 33(4):778–791. <https://doi.org/10.1007/s10409-017-0679-2>
- Cremer L (1948) Über die akustische Grenzschicht vor starren Wänden. *Arch Elek Übertr* 2:136–139
- Dalklint A, Sjövall F, Wallin M, Tortorelli D (2023) Computational design of metamaterials with self contact. *Comput Methods Appl Mech Engrg* 417:116424. <https://doi.org/10.1016/j.cma.2023.116424>
- Dalklint A, Alexandersen J, Frederiksen AH, Poullos K, Sigmund O (2025) Topology optimization of contact-aided thermo-mechanical regulators. *Internat J Numer Methods Engrg* 126(2):e7661. <https://doi.org/10.1002/nme.7661>
- Deaton JD, Grandhi RV (2014) A survey of structural and multidisciplinary continuum topology optimization: post 2000. *Struct Multidiscip Optim* 49(1):1–38. <https://doi.org/10.1007/s00158-013-0956-z>
- Dilgen CB, Dilgen SB, Fuhrman DR, Sigmund O, Lazarov BS (2018) Topology optimization of turbulent flows. *Comput Methods Appl Mech Engrg* 331:363–393. <https://doi.org/10.1016/j.cma.2017.11.029>
- Dilgen SB, Jensen JS, Aage N (2021) Shape optimization of the time-harmonic response of vibroacoustic devices using cut elements. *Finite Elem Anal Des* 196:103608. <https://doi.org/10.1016/j.finel.2021.103608>
- Dong Y, Liu X, Song T, He S (2021) Topology optimization for structure with multi-gradient materials. *Struct Multidiscip Optim* 63(3):1151–1167. <https://doi.org/10.1007/s00158-020-02749-3>
- Dong Y, Hussain I, He S (2025) Structural topology optimization of aircraft wing leading edge fabricated of multilayer composites. *Aerosp Sci Technol* 159:109993. <https://doi.org/10.1016/j.ast.2025.109993>
- Donoso A, Sigmund O (2016) Topology optimization of piezo modal transducers with null-polarity phases. *Struct Multidiscip Optim* 53(2):193–203. <https://doi.org/10.1007/s00158-015-1330-0>
- Du J, Olhoff N (2004) Topological optimization of continuum structures with design-dependent surface loading -Part I: new computational approach for 2d problems. *Struct Multidiscip Optim* 27(3):151–165. <https://doi.org/10.1007/s00158-004-0379-y>
- Du J, Olhoff N (2004) Topological optimization of continuum structures with design-dependent surface loading -Part II: algorithm and examples for 3d problems. *Struct Multidiscip Optim* 27(3):166–177. <https://doi.org/10.1007/s00158-004-0380-5>
- Frederiksen AH, Sigmund O, Poullos K (2024) Topology optimization of self-contacting structures. *Struct Multidiscip Optim* 73(4):967–981. <https://doi.org/10.1007/s00466-023-02396-7>
- Frederiksen AH, Dalklint A, Sigmund O, Poullos K (2025) Improved third medium formulation for 3d topology optimization with contact. *Comput Methods Appl Mech Engrg* 436:117595. <https://doi.org/10.1016/j.cma.2024.117595>
- Fuchs MB, Shemesh NNY (2004) Density-based topological design of structures subjected to water pressure using a parametric loading surface. *Struct Multidiscip Optim* 28(1):11–19. <https://doi.org/10.1007/s00158-004-0406-z>
- Garcia-Rodriguez LF, Kiyono CY, Picelli R, Silva EC (2022) Influence of integer design variables in topology optimization of incompressible turbulent flow. *Appl Math Model* 115:337–359. <https://doi.org/10.1016/j.apm.2022.10.039>
- Glowinski R (1984) Numerical simulation for some applied problems originating from continuum mechanics, mechanics. *Lecture Notes in Physics, trends and applications of pure mathematics to*. Springer, Berlin, Heidelberg
- Glowinski R, Kuznetsov Y (2007) Distributed Lagrange multipliers based on fictitious domain method for second order elliptic problems. *Comput Methods Appl Mech Engrg* 196:1498–1506. <https://doi.org/10.1016/j.cma.2006.05.013>
- Glowinski R, Pan TW, Periaux J (1994) A fictitious domain method for Dirichlet problem and applications. *Comput Methods Appl Mech Engrg* 111:283–303. [https://doi.org/10.1016/0045-7825\(94\)90135-X](https://doi.org/10.1016/0045-7825(94)90135-X)
- Goodman J, Kohn RV, Reyna L (1986) Numerical study of a relaxed variational problem from optimal design. *Comput Methods Appl Mech Engrg* 57(1):107–127. [https://doi.org/10.1016/0045-7825\(86\)90073-3](https://doi.org/10.1016/0045-7825(86)90073-3)
- Groen JP, Sigmund O (2018) Homogenization-based topology optimization for high-resolution manufacturable microstructures. *Internat J Numer Methods Engrg* 113(8):1148–1163. <https://doi.org/10.1002/nme.5575>
- Groen JP, Wu J, Sigmund O (2019) Homogenization-based stiffness optimization and projection of 2D coated structures with orthotropic infill. *Comput Methods Appl Mech Engrg* 349:722–742. <https://doi.org/10.1016/j.cma.2019.02.031>
- Guest JK (2009) Topology optimization with multiple phase projection. *Comput Methods Appl Mech Engrg* 199(1):123–135. <https://doi.org/10.1016/j.cma.2009.09.023>
- Guest JK, Provost JH, Belytschko T (2004) Achieving minimum length scale in topology optimization using nodal design variables and projection functions. *Internat J Numer Methods Engrg* 61(2):238–254. <https://doi.org/10.1002/nme.1064>

- Haertel JH, Nellis GF (2017) A fully developed flow thermofluid model for topology optimization of 3d-printed air-cooled heat exchangers. *Appl Therm Eng* 119:10–24. <https://doi.org/10.1016/j.applthermaleng.2017.03.030>
- Hägg L, Wadbro E (2017) Nonlinear filters in topology optimization: existence of solutions and efficient implementation for minimal compliance problems. *Struct Multidiscip Optim* 55(3):1017–1028. <https://doi.org/10.1007/s00158-016-1553-8>
- Hägg L, Wadbro E (2018) On minimum length scale control in topology optimization. *Struct Multidiscip Optim* 58(3):1015–1032. <https://doi.org/10.1007/s00158-018-1944-0>
- Hammer VB, Olhoff N (1999) Topology optimization with design dependent loads. In: *Proceedings of The 3rd WCSMO : Third World Congress of Structural and Multidisciplinary Optimization*. International Society for Structural and Multidisciplinary Optimization (ISSMO), Buffalo, New York
- Hammer VB, Olhoff N (2000) Topology optimization of continuum structures subjected to pressure loading. *Struct Multidiscip Optim* 19(2):85–92. <https://doi.org/10.1007/s001580050088>
- Hassan E, Wadbro E, Berggren M (2014) Topology optimization of metallic antennas. *IEEE Trans Antennas Propagation* 62(5):2488–2500. <https://doi.org/10.1109/TAP.2014.2309112>
- Hayt WH Jr, Buck JA (2019) *Engineering Electromagnetics*, 9th edn. McGraw-Hill
- Hederberg H, Thore CJ (2025) Fluid–structure interaction topology optimization using density jumps for implicit boundary representation. *Struct Multidiscip Optim* 68(6):122. <https://doi.org/10.1007/s00158-025-04045-4>
- Heijmans HJAM (1995) Mathematical morphology: a modern approach in image processing based on algebra and geometry. *SIAM Rev* 37(1):1–36. <https://doi.org/10.1137/1037001>
- Herrero-Pérez D, Picó-Vicente SG, Martínez-Barberá H (2024) Adaptive density-based robust topology optimization under uncertain loads using parallel computing. *Engrg Comput* 41(1):21–43. <https://doi.org/10.1007/s00366-023-01823-w>
- Høghøj LC, Nørhave DR, Alexandersen J, Sigmund O, Andreasen CS (2020) Topology optimization of two fluid heat exchangers. *Int J Heat Mass Tran* 163:120543. <https://doi.org/10.1016/j.ijheatmasstransfer.2020.120543>
- Hu T, Wang Y, Li H, Yu M, Furuta K, Izui K, Nishiwaki S (2024) Topology optimization of coated structures infilled with multiple materials. *Finite Elem Anal Des* 235:104165. <https://doi.org/10.1016/j.finel.2024.104165>
- Hyman MA (1952) Non-iterative numerical solution of boundary-value problems. *Appl Sci Res* 2:325–351. <https://doi.org/10.1007/BF02919780>
- Ibhadode O, Zhang Z, Rahnama P, Bonakdar A, Toyserkani E (2020) Topology optimization of structures under design-dependent pressure loads by a boundary identification-load evolution (bile) model. *Struct Multidiscip Optim* 62(4):1865–1883. <https://doi.org/10.1007/s00158-020-02582-8>
- Iga A, Nishiwaki S, Izui K, Yoshimura M (2009) Topology optimization for thermal conductors considering design-dependent effects, including heat conduction and convection. *Int J Heat Mass Tran* 52(11):2721–2732. <https://doi.org/10.1016/j.ijheatmasstransfer.2008.12.013>
- Inoue N, Sakuma T (2018) Finite element modeling of acoustic resonators with thermal and viscous boundary layers. *Acoust Sci Tech* 39(5):355–358. <https://doi.org/10.1250/ast.39.355>
- Jihong ZH, Han ZH, Chuang WA, Lu ZH, Shangqin YU (2021) A review of topology optimization for additive manufacturing: Status and challenges. *Chinese J Aeronaut* 34:91–110. <https://doi.org/10.1016/j.cja.2020.09.020>
- Jith J, Sarkar S (2018) Boundary layer impedance model to analyse the visco-thermal acousto-elastic interactions in centrifugal compressors. *J Fluid Struct* 81:179–200. <https://doi.org/10.1016/j.jfluidstructs.2018.05.002>
- Joo Y, Lee I, Kim SJ (2017) Topology optimization of heat sinks in natural convection considering the effect of shape-dependent heat transfer coefficient. *Int J Heat Mass Tran* 109:123–133. <https://doi.org/10.1016/j.ijheatmasstransfer.2017.01.099>
- Joo Y, Lee I, Kim SJ (2018) Efficient three-dimensional topology optimization of heat sinks in natural convection using the shape-dependent convection model. *Int J Heat Mass Tran* 127:32–40. <https://doi.org/10.1016/j.ijheatmasstransfer.2018.08.009>
- Kawamoto A, Matsumori T, Yamasaki S, Nomura T, Kondoh T, Nishiwaki S (2011) Heaviside projection based topology optimization by a pde-filtered scalar function. *Struct Multidiscip Optim* 44:19–24. <https://doi.org/10.1007/s00158-010-0562-2>
- Kohn RV, Strang G (1986) Optimal design and relaxation of variational problems, I. *Comm Pure Appl Math* 39(1):113–137. <https://doi.org/10.1002/cpa.3160390107>
- Kohn RV, Strang G (1986) Optimal design and relaxation of variational problems, II. *Comm Pure Appl Math* 39(2):139–182. <https://doi.org/10.1002/cpa.3160390202>
- Kohn RV, Strang G (1986) Optimal design and relaxation of variational problems, III. *Comm Pure Appl Math* 39(3):353–377. <https://doi.org/10.1002/cpa.3160390305>
- Kreisselmeier G, Steinhauser R (1983) Application of vector performance optimization to a robust control loop design for a fighter aircraft. *Internat J Control* 37(2):251–284. <https://doi.org/10.1080/00207179.1983.9753066>
- Kreissl S, Pingen G, Evgrafov A, Maute K (2010) Topology optimization of flexible micro-fluidic devices. *Struct Multidiscip Optim* 42(4):495–516. <https://doi.org/10.1007/s00158-010-0526-6>
- Kumar P (2023) Topress: a matlab implementation for topology optimization of structures subjected to design-dependent pressure loads. *Struct Multidiscip Optim* 66(4):97. <https://doi.org/10.1007/s00158-023-03533-9>
- Kumar P, Langelaar M (2021) On topology optimization of design-dependent pressure-loaded three-dimensional structures and compliant mechanisms. *Internat J Numer Methods Engrg* 122(9):2205–2220. <https://doi.org/10.1002/nme.6618>
- Kumar P, Frouws JS, Langelaar M (2020) Topology optimization of fluidic pressure-loaded structures and compliant mechanisms using the darcy method. *Struct Multidiscip Optim* 61(4):1637–1655. <https://doi.org/10.1007/s00158-019-02442-0>
- Lagrange JL (1770–1773) *Sur la figure des colonnes*. *Miscellanea Taurinensia* V:123–169
- Lazarov B, Sigmund O (2009) Sensitivity filters in topology optimization as a solution to helmholtz type differential equation. In: *WCSMO-8 8th World Congress on Structural and Multidisciplinary Optimization*
- Lazarov B, Sigmund O (2011) Filters in topology optimization based on helmholtz-type differential equations. *Internat J Numer Methods Engrg* 86(6):765–781. <https://doi.org/10.1002/nme.3072>
- Lazarov B, Alexandersen J, Sigmund O (2014) Topology optimized designs of steady state conduction heat transfer problems with convection boundary conditions. *EngOpt*. <https://doi.org/10.13140/RG.2.2.29361.68966>
- Lazarov B, Wang F, Sigmund O (2016) Length scale and manufacturability in density-based topology optimization. *Arch Appl Mech* 86(1):189–218. <https://doi.org/10.1007/s00419-015-1106-4>
- Lee E, Martins JRRA (2012) Structural topology optimization with design-dependent pressure loads. *Comput Methods Appl Mech Engrg* 233–236:40–48. <https://doi.org/10.1016/j.cma.2012.04.007>
- Li C, Xu C, Gui C, Fox MD (2010) Distance regularized level set evolution and its application to image segmentation. *IEEE Trans Image Process* 19(12):3243–3254. <https://doi.org/10.1109/TIP.2010.2069690>

- Li ZM, Yu J, Yu Y, Xu L (2018) Topology optimization of pressure structures based on regional contour tracking technology. *Struct Multidiscip Optim* 58(2):687–700. <https://doi.org/10.1007/s00158-018-1923-5>
- Lions JL (1971) Optimal control of systems governed by partial differential equations, Die Grundlehren der mathematischen Wissenschaften, vol 170. Springer, Berlin, translated by S. K. Mitter
- Lu Y, Tong L (2021) Topology optimization of compliant mechanisms and structures subjected to design-dependent pressure loadings. *Struct Multidiscip Optim* 63(4):1889–1906. <https://doi.org/10.1007/s00158-020-02786-y>
- Lundgaard C, Alexandersen J, Zhou M, Andreasen CS, Sigmund O (2018) Revisiting density-based topology optimization for fluid-structure-interaction problems. *Struct Multidiscip Optim* 58(3):969–995. <https://doi.org/10.1007/s00158-018-1940-4>
- Luo Y, Li Q, Liu S (2019) Topology optimization of shell-infill structures using an erosion-based interface identification method. *Comput Methods Appl Mech Engrg* 355:94–112. <https://doi.org/10.1016/j.cma.2019.05.017>
- Maute K, Ramm E (1995) Adaptive topology optimization *Struct Opt* 10(2):100–112. <https://doi.org/10.1007/BF01743537>
- Mezzadri F, Qian X (2022) Density gradient-based adaptive refinement of analysis mesh for efficient multiresolution topology optimization. *Internat J Numer Methods Engrg* 123(2):465–504. <https://doi.org/10.1002/nme.6863>
- Michell AGM (1904) The limits of economy of material in frame-structures. *London Edinburgh Dublin Philosoph Magazine J Sci* 8(47):589–597. <https://doi.org/10.1080/14786440409463229>
- Mirpourian J, Aage N (2025) A novel interpolation scheme for strongly coupled multiphysics topology optimization with explicit sensitivity control. *Struct Multidiscip Optim* 68:115. <https://doi.org/10.1007/s00158-025-03972-6>
- Mirpourian J, Aage N (2025a) Arbitrary boundary conditions in topology optimization: Applications in strongly coupled viscothermal multiphysics. 10.21203/rs.3.rs-6690751/v1, preprint, Lab: Ole Sigmund's Lab (the TopOpt Group)
- Mlejnek H (1992) Some aspects of the genesis of structures. *Struct Opt* 5:64–69. <https://doi.org/10.1007/BF01744697>
- Moon H, Kim C, Wang S (2004) Reliability-based topology optimization of thermal systems considering convection heat transfer. In: 10th AIAA/ISSMO Multidisciplinary Analysis and Optimization Conference. American Institute of Aeronautics and Astronautics, Multidisciplinary Analysis Optimization Conferences, <https://doi.org/10.2514/6.2004-4410>
- Mousavi A, Berggren M, Wadbro E (2023) Extending material distribution topology optimization to boundary-effect-dominated problems with applications in viscothermal acoustics. *Mater Design* 234:112302. <https://doi.org/10.1016/j.matdes.2023.112302>
- Mousavi A, Berggren M, Hägg L, Wadbro E (2024) Topology optimization of a waveguide acoustic black hole for enhanced wave focusing. *J Acoust Soc Amer* 155:742–756. <https://doi.org/10.1121/10.0024470>
- Nana A, Cuillière JC, Francois V (2016) Towards adaptive topology optimization. *Adv Eng Sofw* 100:290–307. <https://doi.org/10.1016/j.advengsoft.2016.08.005>
- Nijhof M (2010) Viscothermal wave propagation. PhD thesis, University of Twente, Enschede, The Netherlands
- Niu B, Wadbro E (2021) Multiscale design of coated structures with periodic uniform infill for vibration suppression. *Comput Struct* 255:106622. <https://doi.org/10.1016/j.compstruc.2021.106622>
- Niu B, Yan J, Cheng G (2009) Optimum structure with homogeneous optimum cellular material for maximum fundamental frequency. *Struct Multidiscip Optim* 39(2):115–132. <https://doi.org/10.1007/s00158-008-0334-4>
- Noguchi Y, Yamada T (2022) Topology optimization for acoustic structures considering viscous and thermal boundary layers using a sequential linearized Navier-Stokes model. *Comput Methods Appl Mech Engrg* 394:114863. <https://doi.org/10.1016/j.cma.2022.114863>
- Peskin CS (1972) Flow patterns around heart valves: a numerical method. *J Comput Phys* 10:252–271. [https://doi.org/10.1016/0021-9991\(72\)90065-4](https://doi.org/10.1016/0021-9991(72)90065-4)
- Picelli R, Vicente WRP (2015) Bi-directional evolutionary structural optimization for design-dependent fluid pressure loading problems. *Eng Optim* 47(10):1324–1342. <https://doi.org/10.1080/0305215X.2014.963069>
- Picelli R, Neofytou A, Kim HA (2019) Topology optimization for design-dependent hydrostatic pressure loading via the level-set method. *Struct Multidiscip Optim* 60(4):1313–1326. <https://doi.org/10.1007/s00158-019-02339-y>
- Picelli R, Ranjbarzadeh S, Sivapuram R, Gioria RD, Silva EC (2020) Topology optimization of binary structures under design-dependent fluid-structure interaction loads. *Struct Multidiscip Optim* 62(4):2101–2116. <https://doi.org/10.1007/s00158-020-02598-0>
- Pierce AD (1981) An introduction to Its Physical Principles and Applications. Acoustics. McGraw-Hill
- Postigo JA, Garaigordobil A, Ansola R, Canales J (2024) Topology optimization of shell-infill structures with enhanced edge-detection and coating thickness control. *Adv Eng Sofw* 189:103587. <https://doi.org/10.1016/j.advengsoft.2023.103587>
- Querín O, Steven G, Xie Y (1998) Evolutionary structural optimisation (eso) using a bidirectional algorithm. *Engrg Comput* 15(8):1031–1048. <https://doi.org/10.1108/02644409810244129>
- Sa LF, Yamabe PV, Souza BC, Silva EC (2021) Topology optimization of turbulent rotating flows using spalart-allmaras model. *Comput Methods Appl Mech Engrg* 373:113551. <https://doi.org/10.1016/j.cma.2020.113551>
- Salazar de Troya MA, Tortorelli DA (2018) Adaptive mesh refinement in stress-constrained topology optimization. *Struct Multidiscip Optim* 58(8):2369–2386. <https://doi.org/10.1007/s00158-018-2084-2>
- Saul'ev VK (1963) Solution of certain boundary-value problems on high-speed computers by the fictitious-domain method. *Sibirsk Mat Ž* 4(4):912–925 (In Russian)
- Schmidt K, Thöns-Zueva A (2022) Impedance boundary condition for acoustic time harmonic wave propagation in viscous gases. *Math Methods Appl Sci* 45:7404–7425. <https://doi.org/10.1002/mma.8249>
- Senior TBA (1960) Impedance boundary conditions for imperfectly conducting surfaces. *Appl Sci Res* 8(1):418–436. <https://doi.org/10.1007/BF02920074>
- Setta M, Hägg L, Wadbro E (2024) A boundary strip indicator for material distribution-based topology optimization. *Struct Multidiscip Optim* 67(8):149. <https://doi.org/10.1007/s00158-024-03872-1>
- Sigmund O (1994) Design of material structures using topology optimization. PhD thesis, Technical University of Denmark
- Sigmund O (1997) On the design of compliant mechanisms using topology optimization. *Mech Struct Mach* 25(4):493–524. <https://doi.org/10.1080/08905459708945415>
- Sigmund O (2001) Design of multiphysics actuators using topology optimization—Part I: One-material structures. *Comput Methods Appl Mech Engrg* 190(49):6577–6604. [https://doi.org/10.1016/S0045-7825\(01\)00251-1](https://doi.org/10.1016/S0045-7825(01)00251-1)
- Sigmund O (2001) Design of multiphysics actuators using topology optimization—Part II: Two-material structures. *Comput Methods Appl Mech Engrg* 190(49):6605–6627. [https://doi.org/10.1016/S0045-7825\(01\)00252-3](https://doi.org/10.1016/S0045-7825(01)00252-3)
- Sigmund O (2007) Morphology-based black and white filters for topology optimization. *Struct Multidiscip Optim* 33(4–5):401–424. <https://doi.org/10.1007/s00158-006-0087-x>

- Sigmund O (2009) Manufacturing tolerant topology optimization. *Acta Mech Sinica* 25:227–239. <https://doi.org/10.1007/s10409-009-0240-z>
- Sigmund O, Clausen PM (2007) Topology optimization using a mixed formulation: An alternative way to solve pressure load problems. *Comput Methods Appl Mech Engrg* 196(13):1874–1889. <https://doi.org/10.1016/j.cma.2006.09.021>
- Sigmund O, Maute A (2013) Topology optimization approaches. *Struct Multidiscip Optim* 48(6):1031–1055. <https://doi.org/10.1007/s00158-013-0978-6>
- Sigmund O, Petersson J (1998) Numerical instabilities in topology optimization: a survey on procedures dealing with checkerboards, mesh-dependencies and local minima. *Struct Opt* 16(1):68–75. <https://doi.org/10.1007/BF01214002>
- Sivapuram R, Picelli R (2020) Topology design of binary structures subjected to design-dependent thermal expansion and fluid pressure loads. *Struct Multidiscip Optim* 61(5):1877–1895. <https://doi.org/10.1007/s00158-019-02443-z>
- Smith SM, Brady JM (1997) SUSAN—A new approach to low level image processing. *Int J Comput Vision* 23(1):45–78. <https://doi.org/10.1023/A:1007963824710>
- Spalart P, Allmaras S (1992) A one-equation turbulence model for aerodynamic flows. In: 30th Aerospace Sciences Meeting and Exhibit. American Institute of Aeronautics and Astronautics, Reno, NV. <https://doi.org/10.2514/6.1992-439>
- Svanberg K, Svärd H (2013) Density filters for topology optimization based on the Pythagorean means. *Struct Multidiscip Optim* 48(5):859–875. <https://doi.org/10.1007/s00158-013-0938-1>
- Tian Y, Gao R, Wang Y, Jing R, Li A, Dong X, Hao X (2024) A turbulent flow topology optimization method for diverging tee resistance reduction. *J Build Eng* 97:110609. <https://doi.org/10.1016/j.job.2024.110609>
- Tissot G, Billard R, Gabard G (2020) Optimal cavity shape design for acoustic liners using Helmholtz equation with visco-thermal losses. *J Comput Phys* 402:109048. <https://doi.org/10.1016/j.jcp.2019.109048>
- Verzicco R (2023) Immersed boundary methods: historical perspective and future outlook. *Annu Rev Fluid Mech* 55:129–155. <https://doi.org/10.1146/annurev-fluid-120720-022129>
- Wadbro E, Berggren M (2006) Topology optimization of an acoustic horn. *Comput Methods Appl Mech Engrg* 196:420–436. <https://doi.org/10.1016/j.cma.2006.05.005>
- Wadbro E, Hägg L (2015) On quasi-arithmetic mean based filters and their fast evaluation for large-scale topology optimization. *Struct Multidiscip Optim* 42(5):879–888. <https://doi.org/10.1007/s00158-015-1273-5>
- Wadbro E, Niu B (2019) Multiscale design for additive manufactured structures with solid coating and periodic infill pattern. *Comput Methods Appl Mech Engrg* 357:112605. <https://doi.org/10.1016/j.cma.2019.112605>
- Wallin M, Ivarsson N, Amir O, Tortorelli D (2020) Consistent boundary conditions for pde filter regularization in topology optimization. *Struct Multidiscip Optim* 63(3):1299–1311. <https://doi.org/10.1007/s00158-020-02556-w>
- Wang C, Qian X (2020) A density gradient approach to topology optimization under design-dependent boundary loading. *J Comput Phys* 411:109398. <https://doi.org/10.1016/j.jcp.2020.109398>
- Wang C, Wu Y (2024) Toward static and transient stress-constrained topology optimization for shell-infill structures. *Comput & Structures* 299:107370. <https://doi.org/10.1016/j.compstruc.2024.107370>
- Wang F, Lazarov BS, Sigmund O (2011) On projection methods, convergence and robust formulations in topology optimization. *Struct Multidiscip Optim* 43(6):767–784. <https://doi.org/10.1007/s00158-010-0602-y>
- Wang C, Zhao M, Ge T (2016) Structural topology optimization with design-dependent pressure loads. *Struct Multidiscip Optim* 53(5):1005–1018. <https://doi.org/10.1007/s00158-015-1376-z>
- Wang C, Zhang Y, Yu W, Yang S, Wang C, Jing S (2025) Topology optimization of shell-infill structures for maximum stiffness and fundamental frequency. *Compos Struct* 356:118879. <https://doi.org/10.1016/j.compstruct.2025.118879>
- Wang Z, Zou Z, Zhou Y, Geng X, Sun Y, Huang X, Hao M (2025) Performance comparison of battery cold plates designed using topology optimization across laminar and turbulent flow regime. *Int J Heat Mass Tran* 238:126450. <https://doi.org/10.1016/j.ijheatmasstransfer.2024.126450>
- Wu J, Clausen A, Sigmund O (2017) Minimum compliance topology optimization of shell-infill composites for additive manufacturing. *Comput Methods Appl Mech Engrg* 326:358–375. <https://doi.org/10.1016/j.cma.2017.08.018>
- Wu J, Aage N, Westermann R, Sigmund O (2018) Infill optimization for additive manufacturing—approaching bone-like porous structures. *IEEE Trans Vis Comput Graph* 24(2):1127–1140. <https://doi.org/10.1109/TVCG.2017.2655523>
- Wu J, Sigmund O, Groen J (2021) Topology optimization of multi-scale structures: a review. *Struct Multidiscip Optim* 63:1455–1480. <https://doi.org/10.1007/s00158-021-02881-8>
- Xian Y, Paulino GH, Rosen DW (2025) Integration of additive manufacturing process-induced material characteristics into topology optimization. *Comput Methods Appl Mech Engrg* 434:117503. <https://doi.org/10.1016/j.cma.2024.117503>
- Yang X, Xie Y, Steven G (2005) Evolutionary methods for topology optimisation of continuous structures with design dependent loads. *Comput Structures* 83(12):956–963. <https://doi.org/10.1016/j.compstruc.2004.10.011>
- Yang X, Li H, Gao L (2023) Thermal-mechanical coupling topology optimization of multi-phase infill structures with a non-gradient porosity optimization method. *Int J Heat Mass Tran* 210:124198. <https://doi.org/10.1016/j.ijheatmasstransfer.2023.124198>
- Yang X, Gao L, Li H (2024) Multi-feature parallel topology optimization of fiber-reinforced coated structures based on a dual variable scale filtering method. *Compos Struct* 341:118227. <https://doi.org/10.1016/j.compstruct.2024.118227>
- Yi B, Yoon GH, Peng X (2021) A simple density filter for the topology optimization of coated structures. *Eng Optim* 53(12):2088–2107. <https://doi.org/10.1080/0305215X.2020.1845326>
- Yin L, Ananthasuresh GK (2002) A novel topology design scheme for the multi-physics problems of electro-thermally actuated compliant micromechanisms. *Sens Actuators, A* 97–98:599–609. [https://doi.org/10.1016/S0924-4247\(01\)00853-6](https://doi.org/10.1016/S0924-4247(01)00853-6)
- Yoon GH (2010) Topology optimization for stationary fluid–structure interaction problems using a new monolithic formulation. *Internat J Numer Methods Engrg* 82(5):591–616. <https://doi.org/10.1002/nme.2777>
- Yoon GH (2014) Stress-based topology optimization method for steady-state fluid–structure interaction problems. *Comput Methods Appl Mech Engrg* 278:499–523. <https://doi.org/10.1016/j.cma.2014.05.021>
- Yoon GH (2016) Topology optimization for turbulent flow with spallart-allmaras model. *Comput Methods Appl Mech Engrg* 303:288–311. <https://doi.org/10.1016/j.cma.2016.01.014>
- Yoon GH (2023) A new monolithic design approach for topology optimization for transient fluid–structure interaction system. *Comput Methods Appl Mech Engrg* 403:115729. <https://doi.org/10.1016/j.cma.2022.115729>
- Yoon GH, Kim YY (2003) The role of s-shape mapping functions in the simp approach for topology optimization. *KSME Internat J* 17(10):1496–1506. <https://doi.org/10.1007/BF02982329>
- Yoon GH, Kim YY (2005) The element connectivity parameterization formulation for the topology design optimization of multiphysics

- systems. *Internat J Numer Methods Engrg* 64(12):1649–1677. <https://doi.org/10.1002/nme.1422>
- Yoon GH, Yi B (2019) A new coating filter of coated structure for topology optimization. *Struct Multidiscip Optim* 60:1527–1544. <https://doi.org/10.1007/s00158-019-02279-7>
- Yoon G, Jensen J, Sigmund O (2007) Topology optimization of acoustic–structure interaction problems using a mixed finite element formulation. *Internat J Numer Methods Engrg* 70:1049–1075. <https://doi.org/10.1002/nme.1900>
- Yusuf SN, Asako Y, Sidik NA, Mohamed SB, Japar WM (2020) A short review on rans turbulence models. *CFD Lett* 12(11):83–96
- Yvonnet J, Da D (2024) Topology optimization to fracture resistance: A review and recent developments. *Arch Comput Methods Engrg* 31:2295–2315. <https://doi.org/10.1007/s11831-023-10044-9>
- Zhang H, Zhang X, Liu S (2008) A new boundary search scheme for topology optimization of continuum structures with design-dependent loads. *Struct Multidiscip Optim* 37(2):121–129. <https://doi.org/10.1007/s00158-007-0221-4>
- Zhang B, Zhu J, Gong L, Jia K, Gao L (2023) Topology optimization of heat sink in turbulent natural convection using  $k$ - $\omega$  turbulent model. *Appl Math Model* 118:272–302. <https://doi.org/10.1016/j.apm.2023.01.028>
- Zhou M, Rozvany G (1991) The COC algorithm, Part II: topological, geometrical and generalized shape optimization. *Comput Methods Appl Mech Engrg* 89(1–3):309–336. [https://doi.org/10.1016/0045-7825\(91\)90046-9](https://doi.org/10.1016/0045-7825(91)90046-9)
- Zhou M, Alexandersen J, Sigmund O, Pedersen WCB (2016) Industrial application of topology optimization for combined conductive and convective heat transfer problems. *Struct Multidiscip Optim* 54(4):1045–1060. <https://doi.org/10.1007/s00158-016-1433-2>
- Zhou J, Wang Y, Chiu LN, Ghabraie K (2025) Increasing boundary resolution in topology optimization using a novel formulation of partial elements. *Struct Multidiscip Optim* 68(4):71. <https://doi.org/10.1007/s00158-025-04009-8>
- Zhu J, Zhang W, Xia L (2016) Topology optimization in aircraft and aerospace structures design. *Arch Comput Methods Engrg* 23:595–622. <https://doi.org/10.1007/s11831-015-9151-2>
- Zuo W, Saitou K (2017) Multi-material topology optimization using ordered simp interpolation. *Struct Multidiscip Optim* 55(2):477–491. <https://doi.org/10.1007/s00158-016-1513-3>

**Publisher's Note** Springer Nature remains neutral with regard to jurisdictional claims in published maps and institutional affiliations.